REVIEW ARTICLE

Robotic needle steering: state-of-the-art and research challenges

Mahdieh Babaiasl[1] · Fan Yang[1] · John Paul Swensen[1]

Abstract

Medical robotics is an interdisciplinary field that came into existence to improve medical procedures utilizing robotics technology. Medical robotics range from minimally invasive surgeries using robots to robots that support patients in rehabilitation to image-guided systems for different medical interventions. Different advantages of robots made them appealing to be used for medical interventions. Among these advantages are being precise, untiring, dexterous, and the ability to work in environments that are not safe to human clinicians. Steerable needles are a type of medical devices that can steer around obstacles to reach a target location and thus can improve the accuracy of medical procedures. This paper provides a comprehensive review of the state-of-the-art and research challenges in robotic needle steering. First off, the motivations, including clinical motivations behind needle steering, are demonstrated, and then the state of the art of the different needle steering techniques in the literature are analyzed. This includes their modeling, path planning, control, and clinical applications. Finally, a discussion of the advantages and limitations of the existing techniques that hindered the clinical acceptance of the steerable needles, along with suggestions to get these needles closer to their clinical applications, as well as concluding remarks, is provided.

Keywords Robot-assisted surgery · Steerable needles · Waterjet-assisted surgery · Medical robotics · Soft tissue simulants

1 Motivations behind robotic needle steering

Needles are the least invasive surgical tools used to administer or draw liquids to or from the body. The wound made by a needle is self-healing for most insertion using needles up to 5 mm in diameter [87,94]. Inflexible needles often cannot reach targets in difficult anatomical places without deformation of the needle or the anatomical structure between the insertion point and the destination point. Thus, the need arises for flexible needles that can be steered around the anatomical obstacles, thus improving the placement accuracy of the tip of the needle and improving outcomes for targeted drug delivery and biopsy.

Robotic needle steering allows for the insertion of long flexible needles along curved and controlled paths through soft tissue [39,181]. Robotic needle steering can improve medical interventions in different ways. First off, it allows the clinicians to correct for errors during insertion and reach a target location with increased accuracy compared to the straight insertion. Second, obstacles can be steered around

to avoid anatomical constraints to reach unreachable targets with traditional methods. Third, multiple targets can be reached from a single insertion site, decreasing complications such as bleeding and infection.

The objective of this paper is to provide a comprehensive review of the current research and challenges in robotic needle steering. The paper is organized into four sections. Firstly, we demonstrate the motivations, including clinical ones, behind needle steering, and then analyze the state of the art of the different needle steering techniques in the literature. Our analysis covers modeling, path planning, control, and clinical applications. Finally, the advantages and limitations of existing technologies that prevent steerable needles from becoming clinically accepted are discussed. Suggestions are also provided to help these needles become more clinically viable, as well as concluding remarks.

1.1 Clinical motivation

Some clinical procedures can greatly benefit from robotic needle steering. Examples of these procedures are as follows:

✉ Mahdieh Babaiasl
  mahdieh.babaiasl@wsu.edu

1   Washington State University, Pullman, WA, USA

1.1.1 Liver cancer

Liver cancer is the second leading cause of cancer deaths among men, with about 500 k deaths each year [156]. Radiofrequency ablation (RFA) is the most common procedure for the treatment of liver tumors [89]. In this method, the tumor or other target tissue is thermally destroyed by the heat generated by a high-frequency alternating current at the end effector of a small electrode that can be limited by the needle's maneuverability. Accurate placement of the electrode under image guidance can avoid further dramatic consequences such as hepatic bleeding and destruction of healthy tissues. Approximately three-quarters of the patients are ineligible for surgery, and thus minimally invasive ablations are preferred. Adebar et al. [6,7] stated the need for needles with tighter curvatures to target more points per entry wound that reduces hemorrhage risk. They also stated that a minimum radius of curvature of 50 mm or less is required to ablate liver tumors.

1.1.2 Biopsy for cancer diagnosis

According to the global cancer statistics [156], there were an estimated 10 million deaths from cancer in 2020. Prostate cancer and breast cancer are two of the most prevalent cancers among men, and women, respectively, and lung cancer is the leading cause of death in both men and women. Early diagnosis of the cancer is important for the success of treatment and decrease mortality rates. The biopsy is the common diagnostic method to identify the malignancy of the target tissues. In this method, a needle is used to get small samples of the target tissues for further lab analysis. Accurate placement of the needle is crucial for correct diagnosis since the needle should be placed to sample the malignant tissue instead of healthy tissue. Manual insertions can have different results, and they are highly dependent on the skill and expertise of the physician performing the operation. As a result, robotic needle guidance under visual feedback has a great potential to enhance biopsy performance [160]. Ultrasound (US) feedback and Computerized Tomography (CT) are examples of visual feedback used for performing biopsies [71,192].

1.1.3 Brachytherapy

Brachytherapy is the most effective known treatment for prostate cancer [58] in which the radioactive seeds are placed in the tumors to destroy them. The success of the treatment is dependent on the accurate placement of about 100 small radioactive seeds. In the case of an inaccurate placement, sensitive surrounding tissues like the bladder, rectum, seminal vesicles, or urethra can be destroyed too. Robotic needle guidance can be helpful here, too, since it can be used to perform accurate and repetitive insertions under transrectal

ultrasound guidance [71,150]. Magnetic Resonance Imaging (MRI) can also be used with a robotic needle guidance device [151].

2 Prior work

This section provides a review of the relevant state of the art. First, techniques and design approaches for needle steering in soft tissue are demonstrated. These include tip-based needle steering, fracture-directed needle steering, needle steering using base manipulation, active steerable needles, and needle steering using tissue manipulation. Then, modeling approaches for steerable needles are classified into kinematic models, finite element models, and mechanics-based models. After that, control approaches used in needle steering are discussed. This included control methods used for passive steerable needles and control methods used for active steerable needles. At the end of this section, clinical acceptance of steerable needles is discussed.

It should first be noted that there are steerable catheters such as the ones discussed in [42,43,70,115,144,148,157, 158,170,174,179,180,182] that operate in open spaces through body canals. They are categorized into Continuum robots [76,96,141], Concentric tubes that are made of several telescoping pre-curved superelastic tubes [59,120], and active cannulae [142]. Steering the catheter through open space is fundamentally different from steering the needle through soft tissue, and thus this state of the art is out of the scope of this literature review.

2.1 Techniques, and design approaches for needle steering in soft tissue

From the needle design and its mode of manipulation point of view [165], steerable needles can be classified into *passive* and *active* categories. Passive methods include base manipulation in which lateral translation and rotation motions of the base of the needle are utilized during insertion [56], rotating beveled needle [4,10], pre-curved needle tip [183], pre-bent needle tip [104,154] in which a needle with an asymmetric tip design is used to create curvature, fracture-directed steerable needles [15,190], and notched shaft [73]. Active methods include telescoping cannula [53], programmable bevel [26,106,149,177], tissue manipulation in which deformations of the surrounding tissue are used to alter the position of the target and obstacles [164], and controlled articulating tip [7,166]. Active needles can take into account for any misalignment using their actuation forces. However, they can increase the manufacturing cost and the thickness of the needle. Figure 1, left provides an illustration of the some of the common steering methods in literature.

Fig. 1 (Left) Some common steering methods proposed in the literature. **a** Tip-based steering of a needle with asymmetric tip, **b** base manipulation of a needle with symmetric tip, and **c** base manipulation of a needle with asymmetric tip. Note: tip geometry is not shown in the figure. (Right) Needle tip designs in conventional steerable needles to steer the needle through soft tissue
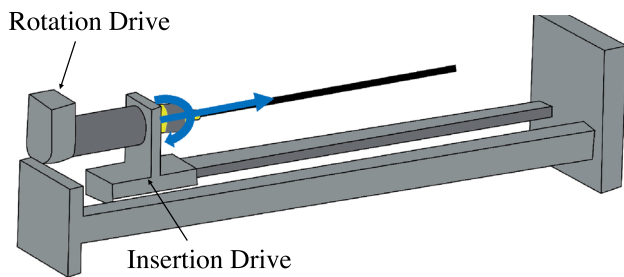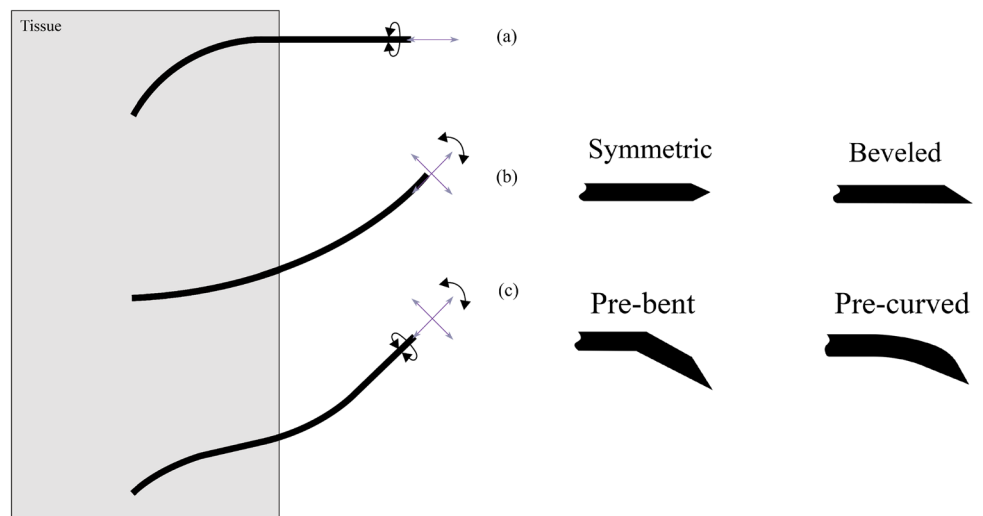
Fig. 2 General concept of the robot insertion device. Recreated from Wesbter et al. [178]

For all techniques of inserting the needles into the soft tissue, an insertion device can insert and rotate the needle and actuate other degrees of freedom where applicable. Figure 2 shows the general concept of the robot insertion device which is recreated from [178].

2.1.1 Tip-based needle steering

Once considered a disadvantage by physicians who would rotate the needle at the base to avoid its deflection, tip-based needle steering use this as an advantage for steering. Tip-based steering methods use the asymmetry of the needle tip (bevel tip, pre-curved or pre-bent tip) to create forces at the tip needed to steer the needle (see Fig. 1, right). These needles are usually made of Nitinol, which is a superelastic alloy of nickel and titanium. This allows the needle to be more flexible than straight needles relative to the surrounding tissue, which allow for deflection of the needle as it cuts into the tissue.

The resultant needle deflection has been described using kinematic models. Some of these first kinematic models proposed by Webster et al. [181] apply to tip-based steerable needles. Control of the needle is accomplished through 2

degrees of freedom (DOF): insertion and rotation of the needle at its base along the central axis.

Duty cycling control strategy [45,110] uses the cycles of pure insertion of the needle (maximum curvature) and insertion with continuous rotation (straight path) to control the curvature of the tip-based steerable needles. The resulting needle tip path can be approximated by an arc of a circle with an effective curvature κ_{eff} that can be tuned between 0 and the maximum curvature κ_{max}. The relationship between κ_{eff}, and the duty cycle ratio DC can be approximated by the following linear function [110]:

$$\begin{aligned} \text{DC} &= \frac{\ell_{\text{rot}}}{\ell_{\text{rot}} + \ell_{\text{ins}}} \\ \kappa_{\text{eff}} &= (1 - \text{DC})\kappa_{\text{max}} \end{aligned} \tag{1}$$

where ℓ_{ins}, and ℓ_{rot} are the insertion lengths of the pure insertion and insertion with continuous rotation, respectively. If the insertion velocity is constant, then the duty cycle DC can be found from each phase's duration instead of their insertion length [20,29,109,128,169,185]. The limitations of the duty cycle control are as follows. First, the maximum curvature κ_{max} should be known beforehand to compute DC. This parameter is difficult to find in practice, and an online estimation scheme is required [117]. The other limitation is that continuously rotating the needle along its axis is not always possible, especially when sensors or trackers are embedded in the needle.

The effect of the bevel angle on needle path has been studied in artificial tissue simulants [178], ex vivo tissues [104], and in vivo soft tissues [101]. For bevel-tip-steerable needles, the smaller the bevel angle, the smaller the radius of curvature [146]. The curvature of the bevel-tip-steerable needles in very soft and biological tissues is very low, limiting the use of duty cycle control in clinical practice. In order to increase the curvature of the needle, pre-bent tips [7], and pre-curved tips

[168] are introduced. However, these needle tips are not suitable for duty cycling control due to increased tissue damage during the rotation of the needle. Needle curvature depends on the needle material properties, tissue material properties, tip bevel angle, and friction between the needle's shaft and surrounding tissue.

Webster et al. [178] developed a robotic needle steering device that includes force/torque sensor, horizontal needle insertion, and stereo image data acquisition. They showed that the needle path is not dependent on insertion velocity during experiments in tissue phantoms but depends on bevel-tip angle.

They also measured the forces acting on the needle during insertion and showed that they depend on the insertion velocity. The rubber-like Simulated Muscle Ballistic Test Media from Corbin, Inc. is used as the soft tissue simulant. The tissue simulant is fairly stiff with a stiffness of 4.9 $\frac{N}{mm}$ by a blunt indentation test and applies less friction to the shaft of the needle in comparison to similar phantoms like silicone with similar stiffness. The stiffness of the soft tissue used is more than most human soft tissues. The needle used is a 0.83 mm diameter Nitinol (an alloy of 55% Nickel and 45% Titanium, and when heat-treated becomes a superelastic material) with a hand-machined bevel tip with 40° angle. Bevel angle has little effect on the axial force. Steering is improved (smaller radius of curvature) with decreasing bevel angle down to 5°.

Misra et al. [114] obtained the minimum radius of curvature of 179.4 mm (which is quite high) with 0.4 mm pre-curved needle in Plastisol soft tissue phantoms with plastic to softener ratio of 4:1. Park et al. [125] used a beveled tip needle of 0.57 mm diameter in Plastisol soft tissue phantoms with plastic to softener ratio of 4:1 and achieved a radius of curvature of 161.3 mm. Reed et al. [132] used a 15° pre-bent needle with a beveled tip of 45° with 0.61 mm diameter in Plastisol soft tissue phantoms with plastic to softener ratio of 4:1 and achieved a radius of curvature of 61 mm. Majewicz et al. [104] used a pre-bent needle tip with 0.58 mm diameter and achieved a minimum ROC of 34 mm in goat liver. They found that a bevel-tip needle with a diameter of 0.58 mm obtains a 667 mm minimum radius of curvature. Wedlick and Okamura [183] used pre-curved needles with 0.48 mmm diameter made of Nitinol and obtained a minimum ROC of 15.5 mm in Plastisol rubber with a 4 to 1 ratio of regular stiffness plastic to plastic softener as a phantom tissue. However, they stated that the methods of needle fabrication are not perfectly repeatable. The curvature can only be controlled by duty cycling, which causes considerable tissue damage.

Okazawa et al. [122] proposed a hand-held steerable needle of 0.902 mm diameter consisting of a pre-bent stylet inside a straight cannula. They concluded that the curvature of the needle path increases as the phantom stiffness and needle extension increase. Stiffer tissues generate a more immediate lateral reaction against the curved portion of the

stylet, resulting in a greater curvature. Tissue-mimicking phantoms are made of polyvinyl chloride compound. The insertion velocity is 5 $\frac{mm}{s}$. They showed that changing the insertion speed within the range of the velocities used in clinical practice (1–10 $\frac{mm}{s}$) did not change the tip path curvature. Their steering method is based on the fact that the cannula must be stiffer than the stylet, and the tissue must be stiffer than the cannula. This limits the achievable smaller radius of curvature. They obtained the maximum lateral deflection of 35 mm in tissue with an elastic modulus of 157 kPa, and with a 12 mm extension of the inner stylet.

Swaney et al. [159] designed a flexure-based needle tip that provided the high curvature of the pre-bent needles during insertion and low tissue damage of the bevel-tip needles during rotations. Duty cycling is used to control the curvature of the needle. The outer diameter (OD) and the inner diameter (ID) of the needle are 0.91 mm and 0.6 mm, respectively, with 10° bevel angle. The tip flexes to the maximum angle of about 22°. The tissue phantoms used for the experiments are made of 10% by weight Knox Gelatin (Kraft Foods Global Inc., IL), and ex vivo pork loin. They found that curvature decreases linearly by increasing duty cycle rate with the curvature of 0 for 100% duty cycling (constant axial rotation) and maximum curvature for 0% duty cycling (no axial rotation). The velocity of insertion into soft tissues is 0.5 $\frac{cm}{s}$. They got a minimum radius of curvature (0% duty cycle) of 12.1 cm in gelatin phantoms and 17.6 cm in ex vivo pork loin. Figure 3 shows the proposed steerable needle.

Lee et al. [86] proposed a tube-wire type flexible steerable needle with variable curvature. The design consists of the inner pre-bent wire and an outer tube. The needle is controlled from the base inputs (insertion and rotation commands). The performance of the needle is tested in ballistic gelatin and animal tissue samples. The wire has a 0.8 mm diameter, and the outer tube is of 1 mm inner diameter (ID) and 1.2 mm outer diameter (OD). The extension length of the wire can control the curvature. They obtained a minimum radius of curvature of 20 mm in ballistic gelatin. They obtained the minimum radius of curvature of 104.5 mm in cow liver and 18.6 mm in beef. Figure 4, left gives an illustration of the proposed design by Lee et al. [86].

Bui et al. [24] proposed a variation of the bevel-tip-steerable needles with an "airfoil" tip. This steerable needle does not need duty cycling to control its curvature. The proposed needle consists of a stylet with a bevel tip and a cannula, and the curvature of the needle path can be controlled by varying the control offset (the amount of the stylet retraction). The needle has an OD of 0.46 mm and is tested in vitro gelatin soft tissue phantoms and ex vivo cow liver tissue. The minimum radii of curvature are 125 mm, 72 mm, and 263 mm in 6% by weight gelatin phantom, 10% by weight gelatin phantom, and cow liver, respectively. They experimentally showed that
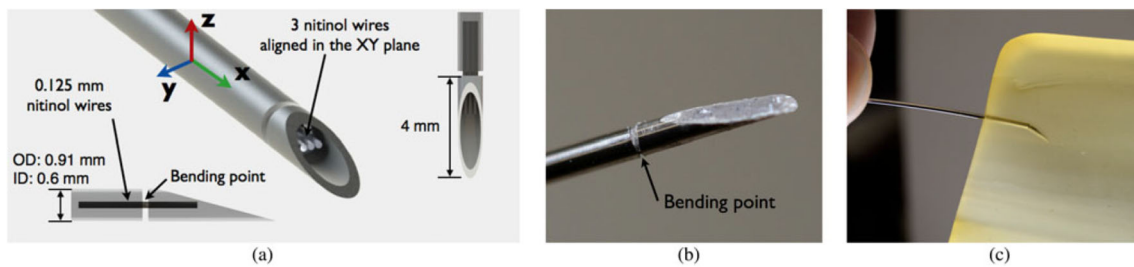
Fig. 3 Flexure-tip-steerable needle proposed by Swaney et al. [159]. **a** CAD model of the flexure-tip needle with the dimensions. **b** Flexure-tip-steerable needle prototype. **c** When the flexure-tip needle is inserted into the tissue it bends due to reaction forces from the tissue. It remains straight during the duty cycling control. © 2013 IEEE
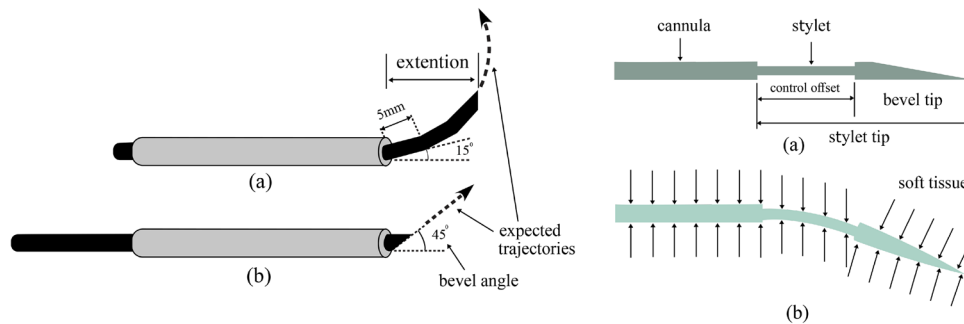
Fig. 4 (Left) Wire and tube steerable needle illustration recreated from the design proposed by Lee et al. [86]. **a** Full extension, and **b** Full retraction. The curvature is controlled by varying the extension length of the wire. (Right) "Airfoil" bevel needle with varying stylet offset illustration recreated from [24]. **a** Needle's design, and **b** Needle under applied forces from surrounding soft tissue. The curvature can be controlled by changing the control offset

the curvature is a linear function of the control offset. Figure 4, right shows the proposed steerable needle.

Khadem et al. [75] proposed a way to decrease the bending stiffness of the tip-steerable needles and thus increasing the maximum achievable curvature by adding one or more notches on the needle shaft. The notched needle design achieved a minimum radius of curvature of 198 mm in Plastisol soft tissue phantoms (80% liquid plastic and 20% plastic softener resulting in elastic modulus of 35 kPa), which is 67% better than standard needles. In another study, Khadem et al. [73] used a notched needle tip and achieved a minimum Radius of Curvature (ROC) of 171 mm by increasing the number of notches in Plastisol soft tissue phantoms.
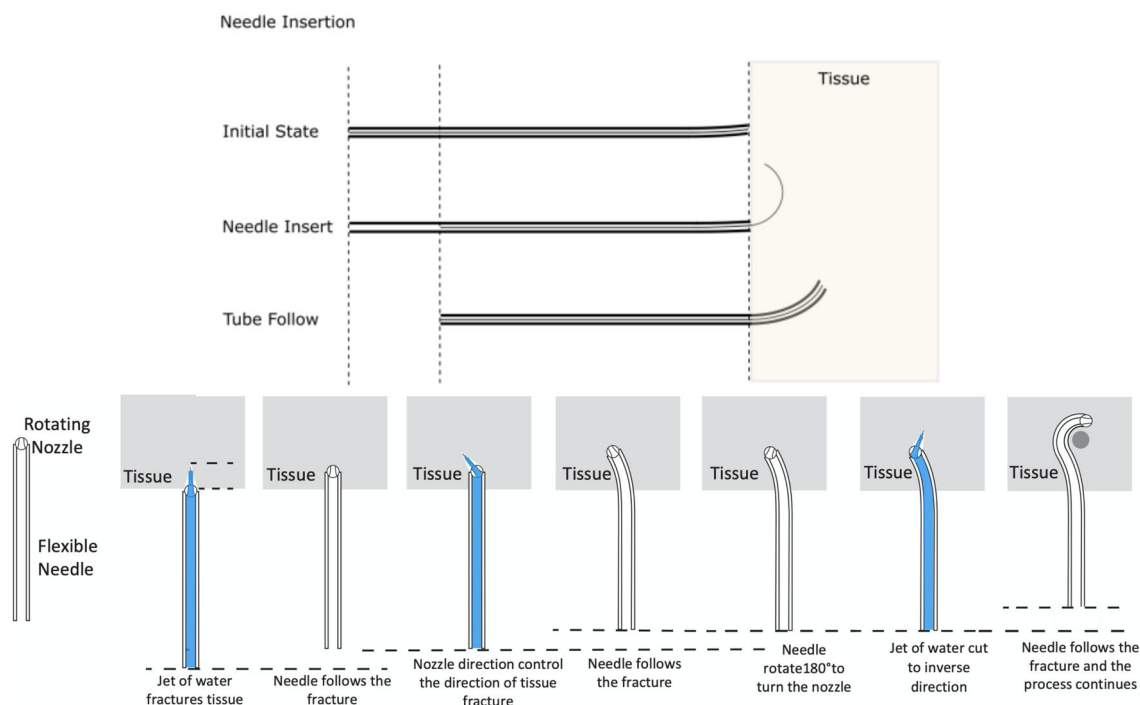
2.1.2 Fracture-directed needle steering

Yang et al. [190] developed a new method of needle steering called "fracture-directed needle steering," in which the objective is first to control the direction of tissue fracture and then have the needle follow the fractured path. The principle of fracture-directed steering promised the potential of a significantly improved radius of curvature and steerability that is currently attainable with tip-steerable needles.

Figure 5, up describes the principle of the stylet-and-tube form of fracture-directed steerable needles, where an inner stylet with a predefined geometry is first extended from the tube to fracture the tissue, after which the tube follows the stylet along the fracture direction.

The proposed fracture-directed needle steering method consists of a straight outer elastic tube and an inner elastic wire stylet. Silicon rubber 15%, and 20% SEBS soft tissue simulants are used as tissue-mimicking materials for needle steering experiments. The lowest insertion radius attained in experiments with silicone compound tissue phantom ($E = 687$ kPa) using Nitinol tube (Tube ID = 0.6, OD = 0.8, and needle diameter = 0.47 mm), and SEBS tissue phantom ($E = 128$ kPa) using SemiFlex tube (tube OD = 1.45, ID = 0.7, and needle diameter = 0.47 mm) are 29.58 mm, and 6.88 mm, respectively.

Another possible implementation of the fracture-directed steerable needles is waterjet steerable needles [14,16,17] in which the direction of the tissue fracture is controlled by waterjet coming through an angled nozzle, and then the flexible needle follows the fractured path. Figure 5, down shows the underlying principle of the waterjet steerable needles, in which the direction of the tissue fracture is controlled by angled waterjet, and then the flexible Nitinol tube follows.

Fig. 5 (Up) Principle of fracture-directed stylet-and-tube steering. First, the inner stylet is advanced, followed by the outer tube. After the outer tube follows the inner stylet, the resulting tip position depends on the static equilibrium of the wire, tube, and tissue. (Down) Underlying Principle of the Waterjet Steerable Needles. First, the tissue fracture direction is controlled by an angled sub-millimeter waterjet, and then the flexible Nitinol tube follows the cut path. This process continues till the needle avoids the obstacles and reaches a target location

This process continues until the waterjet needle reaches a target location avoiding obstacles.

2.1.3 Needle steering using base manipulation

Base manipulation is controlling the needle tip trajectory using control of the 6 DOFs of the needle base. This is shown in Fig. 1b, c. This is the natural way physicians use to steer a needle when holding it by its base. Dimaio et al. [39] first introduced the method of controlling the needle from its base. They performed the steering in an open-loop. Glozman and Shoham [54] performed closed-loop needle base manipulation under fluoroscopic feedback, and Neubah and Shoham [119] did it under ultrasound guidance. Bending the needle and pushing on the tissues to control the tip's lateral motion, which is used in the base manipulation method, can potentially induce more tissue damage than only inserting the needle. This limits the use of base manipulation in real-world scenarios.

2.1.4 Active steerable needles

Ayvali et al. [13] proposed an active segmented cannula with pre-curved SMA wires. They evaluated the proposed needle in Knox Gelatin. The cannula has a 1.4 mm inner diameter

(ID) and 3 mm outer diameter (OD). Black et al. [23] developed active needles with two degrees of freedom (DOF) with a single SMA wire. They evaluated the needle in a tissue phantom simulating the mechanical properties of the human prostate. No curvature data is given in the paper.

Konh and Podder [83] developed an active needle actuated by a single SMA wire and showed the efficacy of the needle through 2D experiments [82]. The needle is evaluated in air and a tissue-mimicking gel. The tissue-mimicking gel is made of Plastisol with a 3 : 1 ratio of plastic (polyvinyl chloride suspension) to the softener. The velocity of insertion into the tissue is 2.54 $\frac{mm}{s}$, and the maximum needle deflection is about 32 mm in gels. The overall diameter of the needle is 2.6 mm. Konh et al. [81] 3D manipulated an active steerable needle via actuation of three SMA wires. The experiments are conducted in free space and not in the soft tissue. Curvature can be controlled by changing the applied current to the actuator wire.

There are also steerable needles that can be steered by cable actuation. These needles are capable of on-demand steering at the tip in one plane [7,52], or on-demand steering in two perpendicular planes [98,166], and changing of the needle trajectory "on the spot" [147]. Cable-actuated steerable needles allow for a high level of maneuverability. They are still more complex, and diameters need to be larger than

1 mm since smaller diameters lead to smaller moment arms, and higher actuation force will be needed.

Scali et al. [147] developed a needle with a 0.5 mm probe that can steer in 3D without the need for axial rotations. The needle consists of 3 Nitinol wires, each with a diameter of 0.125 mm with a pre-curved tip inside a stainless steel tube. They tested the needle's efficacy in 10% by weight Gelatin soft tissue phantoms (they obtained a Young's Modulus of 17 kPa). Their design is a combination of the cable-actuated needles with the pre-bent needles. The insertion speed of the experiments is $2 \frac{mm}{s}$. Tip angles can only be 10°, 20°, and 50°. Figure 6, left shows the proposed design.

Van de Berg et al. [166] used four actuation cables running alongside the shaft and connecting to the tip to change the tip's angle (refer to Fig. 6, right). They obtained a minimum ROC of 181 mm. Fiber Bragg Gratings (FBGs) are used to sense and measure the needle shape and tip position during operation. PI-controller is used to steering to predefined targets. They achieved a targeting accuracy of 6.2 ± 1.4 mm (mean ± std), and steering precision of 2.6 ± 1.1 mm in 15% gelatin soft tissue phantoms with Young's moduli of 10 kPa which is in the order of the stiffness of the liver (it should be noted that the tissue stiffnesses are variable among the literature due to variability in techniques and test conditions). The needle consist of a 0.5 mm radius (r_1) stainless steel stylet, and 0.9 mm radius (r_2) PEEK plastic cannula. The outer needle radius is approximately 1 mm. 4 actuation cables are fixed at the tip, and each connects to one servo motor. The velocity of insertion during experiments is $5 \frac{mm}{s}$.

Burrows et al. [26] developed a complex needle with 4 actuated shafts to change the tip geometry and obtained a minimum ROC of 58 mm. Adebar et al. [8] developed an actuated hinge near the needle tip and achieved a minimum ROC of 55.8 mm in ex vivo liver with 16 mm tip length. They showed that increasing the tip length and tip angle decreases the achieved minimum radius of curvature. They obtained the minimum radius of curvature of 46.7 mm with a tip angle of 60°.

Ilami et al. proposed a magnetic needle steering method [64] (see Fig. 7). Unlike the traditional needle techniques that depend on the radial forces and rotation at the base of an asymmetric tip needle for steering, and another magnetic steering of catheters, and continuum robots that rely on mechanical or manual shaft advancement methods, this method uses magnetic forces and torques to both steer and advance a sharp magnetic tip.

In this method, the needle is magnetically pulled rather than mechanically pushed, avoiding buckling and obtaining minimal Radius of Curvature (ROC). The needle tip has a diameter of 1.59 mm. They obtained a minimum ROC of 10.2 mm. Their system has the ability of variable Radii of Curvature without duty cycling; therefore, it does not need rotation for steering.

A possible disadvantage is prolonged human exposure to powerful magnetic fields [131]. Because of the limitations on magnetic field strength, they have chosen soft tissue stiffnesses that are lower than human soft tissues. They have examined two soft tissue phantoms with 1.96 (1.2 g of agar gelling powder and 0.08 g of pure agarose powder per 100 mL of distilled water), and 2.70 (1.6 g of agar gelling powder and 35 µg of pure charcoal per 100 mL of distilled water) kPa stiffnesses, respectively.

Dalta et al. [32] proposed a flexure-based active needle for needle steering in soft tissue. Needle curvature is controlled by shape memory alloy (SMA) wires applying actuator forces to bend the needle. They evaluated the needle in air, tissue-mimicking gel [polyvinylchloride (PVC) gel with 3:1 ratio of plastic (PVC suspension) to softener with an elastic modulus of 25.6 kPa comparable to the elastic modulus of normal prostate tissue (22.74 kPa)], and ex vivo pig liver. The needle consists of two hollow tubes, an actuator wire, a flexible connector, and a needle tip. The hollow tubes are made of superelastic Nitinol of 2.2 mm OD and 1.7 mm ID. The velocity of insertion is $2.54 \frac{mm}{s}$. The applied current can control the bend angle of the SMA wire. The maximum deflection of the needle in pig liver and gels is 41.9 mm, and 29.5 mm, respectively.

Roesthuis et al. [139] proposed a flexible steerable needle with a tendon-driven actuated tip. Fiber Bragg Grating (FBG) sensors are used to measure the needle tip pose. The needle's performance is evaluated in porcine gelatin soft tissue phantoms (14.9% by weight with Young's modulus of 35 kPa, which is in the order of the stiffness of human breast tissue). The needle tip has a conical shape with a length of 5 mm. The tip is on the ball joint, and four steering tendons are used to actuate the tip. The needle is made of a Nitinol stylet of diameter 1 mm, and a PEEK plastic cannula of 2 mm diameter. The velocity of insertion in experiments is $5 \frac{mm}{s}$. Maximum curvature is obtained with an angle of 15° resulting in a minimum radius of curvature of 200 mm.

2.1.5 Needle steering using tissue manipulation

Needle steering using tissue manipulation is done by deforming the tissues' internal parts by moving one [164], or multiple points [105,127] of the surface of the tissues. Accurate finite element modeling (FEM) of the tissues is required for this type of control, difficult to obtain in practice. On the other hand, the computational burden of the FEM also hinders its real-time use that limits the pre-planning. Tissue manipulation is only used to move superficial targets and not deep anatomical structures.

Fig. 6 (Left) Steerable needle designed by Scali et al. [147] © 2019 Scali et al. (**A**, **B**) with its actuation unit (**C**). (Right) The tendon-driven needle proposed by Van de Berg et al. [166] © 2015 ElSEVIER. FBG sensors are used to sense and recreate the shape of the needle and measure the tip position during insertions. ϕ can be up to 20°
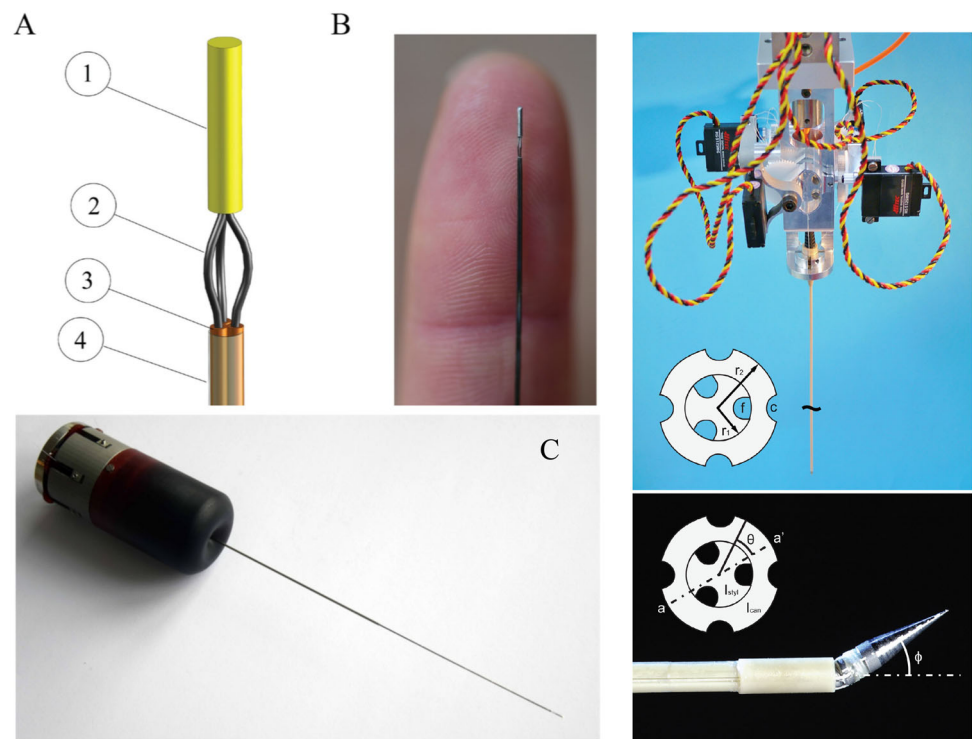
Fig. 7 Magnetic Needle steering system proposed by Ilami et al. [64] © The Authors 2020
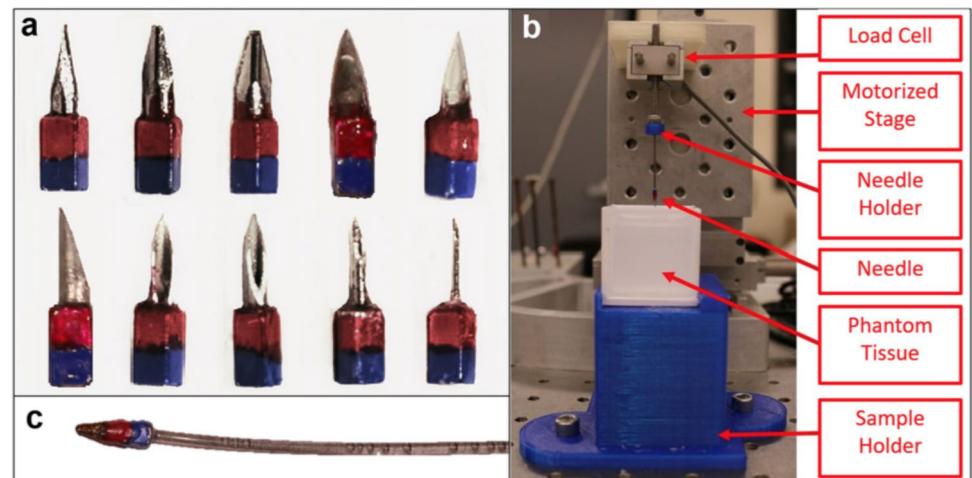
2.2 Modeling approaches for steerable needles

Needle-tissue interaction models provide an understanding of the flexible needle interacting with soft tissue. This understanding is helpful in the sense that the needle path can be predicted before actual needle insertion. This can help predict the behavior of the steerable needle in reaching the targets. Needle modeling approaches can be classified into kinematic models, which consider the trajectory of the needle tip, finite element models that can model the behavior of the needle and the tissue, and mechanics-based models. Developing accurate models are also important to construct efficient controllers and estimators.

2.2.1 Kinematic models

Webster et al. [181] proposed and validated a nonholonomic model for bevel-tip needle steering. The model is a generalization of the 3 DOF nonholonomic unicycle and bicycle models to 6 DOF using Lie group theory. The models are validated using experiments with a needle insertion device into soft tissue phantoms. They used a 0.7 mm diameter needle with a bevel angle of 45°. Soft tissue phantoms used are Simulated Muscle Ballistic Test Media (SimTest) from Corbin, Inc. The stiffness of this soft tissue simulant is similar to the muscle (4.9 N/mm). They found that the root mean squared error between the model prediction and the observed data

points is 1.3 mm for the bicycle model and 2.6 mm for the unicycle model, concluding that the two-parameter bicycle model describes the needle behavior better than a single-parameter unicycle model. Figure 8 shows the definition of the bicycle and unicycle model proposed by Webster et al. [181].

These models are summarized as follows:

$$\dot{g}_{ab}^{-1}(t)g_{ab}(t) = u_1\hat{V}_1 + u_2\hat{V}_2$$
$$V_1 = \begin{bmatrix} e_3 \\ \kappa e_1 \end{bmatrix}, V_2 = \begin{bmatrix} 0 \\ e_3 \end{bmatrix}$$
$$n(t) = R_{ab}(t)\ell_2 e_3 + p_{ab}(t), \text{ for bicycle model}$$
$$n(t) = p_{ab}(t), \text{ for unicycle model } (\ell_2 = 0)$$

(2)

where κ, u_1, u_2, g_{ab}, R_{ab}, p_{ab}, $\hat{}$, e_1, e_2, and e_3 are curvature, insertion, and rotational velocities, transformation matrix, rotational matrix, position matrix, the relationship between R^3 and the Lie algebra of SE(3), and unit vectors, respectively. $n \in R^3$ is the needle tip position.

It can be demonstrated that the needle tip pose can be calculated using the following Eq. [181]:

$$\begin{bmatrix} \dot{x} \\ \dot{y} \\ \dot{z} \\ \dot{\alpha} \\ \dot{\beta} \\ \dot{\theta} \end{bmatrix} = \begin{bmatrix} \sin(\beta) & 0 \\ -\cos(\beta)\sin(\alpha) & 0 \\ \cos(\alpha)\cos(\beta) & 0 \\ \kappa\cos(\theta)sec(\beta) & 0 \\ \kappa\sin(\theta) & 0 \\ -\kappa\cos(\theta)\tan(\beta) & 1 \end{bmatrix} \begin{bmatrix} u_1 \\ u_2 \end{bmatrix}$$

(3)

where $q = \begin{bmatrix} x & y & z & \alpha & \beta & \theta \end{bmatrix}^T$ is the generalized coordinates for the needle tip position and orientation, and κ is the radius of curvature of the needle path. This equation is especially suitable for control purposes.

Minhas et al. [110] proposed a kinematic model to describe passive steerable needles' trajectory with duty-cycled spinning. Duty-cycled spinning is the approach to control the curvature of the passive steerable needles from the natural curvature of the needle in the soft tissue to zero curvature. They validated the model in Knox Gelatin (1.3 cc of Gelatin in 20 cc of water) tissue simulants, which has a similar insertion force profile to that of the brain tissue in vitro. The minimum radius of curvature obtained in Knox Gelatin is 5 cm, and it is found that the curvature decreases linearly with the duty cycle. The needle used in the experiments is a custom-made needle with a 1.27 mm diameter stainless steel hypodermic needle tip attached to a 0.28 mm diameter Nitinol wire. The bevel angle is 10° and is bent an additional 15° at a distance of 6.3 mm from the end of the tip. The proposed kinematic model is as follows:

$$g(t) = \begin{cases} g(0)e^{(u_1\hat{V}_1 + u_2\hat{V}_2)t}, & jT \leq t < T(j+D), j = 0, 1, 2, ... \\ g(0)e^{u_1\hat{V}_1 t}, & \text{else} \end{cases}$$
$$n(t) = R(t)l_2 e_3 + p(t)$$

(4)

where T, l_2, u_1, u_2, $g(0)$, $R(t)$, $p(t)$, and V_1, $V_2 \in R^6$ are duty cycle period, back wheel to needle tip distance in bicycle model, insertion speed, rotational speed, initial configuration of the needle, rotational component of the needle configuration, translational component of the needle configuration, and twist coordinates of the twists $\hat{V}_1$, $\hat{V}_2 \in$ se(3). $V_1 = \begin{bmatrix} 0 & 0 & 1 & \kappa & 0 & 0 \end{bmatrix}^T$, and $V_2 = \begin{bmatrix} 0 & 0 & 0 & 0 & 0 & 1 \end{bmatrix}^T$. e_3 is the z-coordinate unit vector.

Yang et al. [190] presented a discrete analog of the bicycle model for the proposed method of stylet-and-tube fracture-directed needles. In this model, the independent variable is the stylet's step length before following with the tube. Consider a pre-curved stylet that is driven by step length from the end of the tube. As the stylet exits the tube and enters the tissue, the stylet will nominally follow the stylet's predefined shape. The step length is modeled as the input to the system. A mathematical model is developed for the needle tip position with respect to the base frame as a function of the step length, and it is fit to the experimental data. Figure 9 shows the three distinct stages of needle insertion into the tissue. First, the stylet is extended out of the tube, after which the tube follows the stylet. The z-axis of the body-fixed frame is the direction of insertion. The arc length of each step is parameterized by l, in millimeters.

The twist coordinates of the system are defined as follows:

$$\xi(l) = \begin{bmatrix} \omega \\ v \end{bmatrix} = \begin{bmatrix} \kappa(l) \\ 0 \\ 0 \\ 0 \\ 0 \\ 1 \end{bmatrix}$$

(5)

The twist describes the discrete-step needle motion and is a function of l, which is the length of the needle inserted before the tube follows. By inspection of the vector field defined by the twist, the needle system has rotation around the body-fixed x-axis and linear translation along the z-axis. The pose of the needle after a step is calculated as the product of matrix exponential of the twist and the previous pose using the matrix exponential of the twist describing the motion in each discrete step of the stylet and tube:

$$g_{k+1} = e^{\hat{\xi}_k l} g_k.$$

(6)

Fig. 8 Unicycle and Bicycle kinematic models for asymmetric tip needles (bevel-tip and pre-curved needles) proposed by Webster et al. [181]. Translation and rotation of the wheels are shown with straight and curved arrows, respectively. For the Bicycle model, the rotation occurs naturally, but the rotation should be added artificially for the unicycle model

(a) Unicycle model

(b) Bicycle model
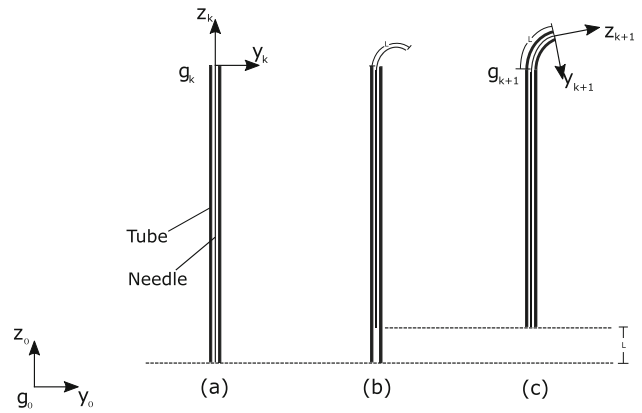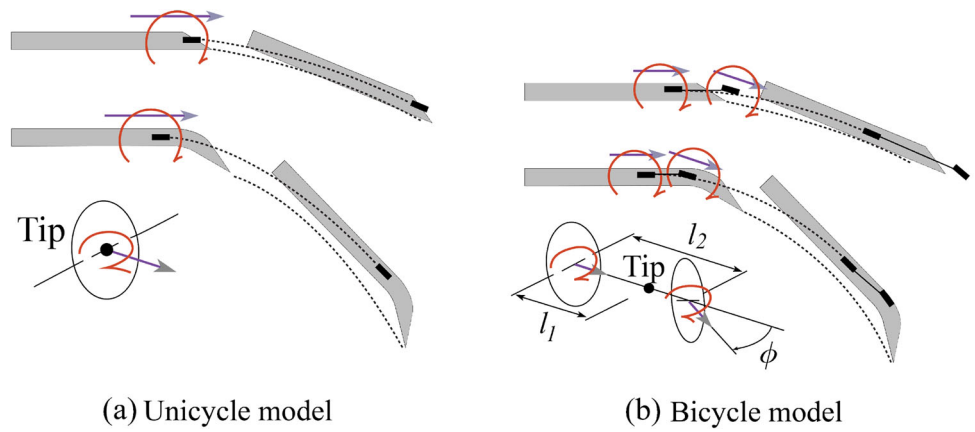
Fig. 9 Position and orientation of the needle tip in the kinematic model proposed by Yang et al. [190]

The discrete-step position/ orientation change is only a function of the length of the needle inserted before the tube follows. The matrix $g_k \in$ SE(3) is the tube tip position/orientation before the needle is inserted, and $g_{k+1} \in$ SE(3) is the tube tip position/orientation after the needle has been inserted and the tube has followed.

Babaiasl et al. [14,15] developed a kinematic model for waterjet steerable needle motion. It consists of a mechanics-based model for predicting the depth of cut of the waterjet in soft tissue and a kinematics model to describe the needle path using this computed depth of cut.

A mechanics-based model for the depth of cut of the waterjet in soft tissue that predicts the depth of cut based on tissue mechanical properties (constitutive response and fracture toughness), as well as waterjet properties (diameter and velocity) is developed by Babaiasl et al. [14]. To summarize: the cut-depth of the waterjet in soft tissue can be expressed by the following ordinary differential equation, where A_{surf} and A_{out} are functions of h and their equations are given in [14]. This equation can be readily integrated using standard

methods such as Runge–Kutta integrators:

$$\frac{dh}{dt} = \frac{1}{P_w} \frac{\rho Q^3}{\pi^3 R^6} \frac{A_{inj} A_{surf}}{(A_{surf} + A_{out})^2} \tag{7}$$

Here, h is the depth of cut and P_w, ρ, Q, R, A_{inj}, A_{surf} and A_{out} are penetration pressure of the waterjet (Pa), density of the water ($\frac{kg}{m^3}$), volumetric flow rate of the waterjet ($\frac{m^3}{s}$), needle inner radius (in their case: $2R = 0.24$ mm) and injection, surface and backflow areas (m^2), respectively. The penetration pressure of the waterjet in soft tissue can be expressed by the following equation:

$$P_w = \frac{4}{D \left(1 - \left(\frac{d}{D}\right)^2\right)} \left\{ J_{IC} \left(\frac{d}{D}\right) + \frac{D}{4} \frac{2\mu}{\alpha^2} \left[\int_1^\infty f\left(\frac{d}{D}, \gamma\right) d\gamma \right. \right.$$
$$\left. \left. + 2\left(\frac{d}{D}\right)^{2-\alpha} + \left(\frac{d}{D}\right)^{2\alpha+2} - 3\left(\frac{d}{D}\right)^2 \right] \right\}, \tag{8}$$

where D, d, J_{IC}, α, μ, ρ, v and T are waterjet diameter, steady-state diameter after waterjet removal, mode I fracture toughness, strain hardening factor, shear modulus, water density, waterjet velocity and time, respectively. Function $f(\frac{d}{D}, \gamma)$ can be expressed in the closed-form as:

$$f\left(\frac{d}{D}, \gamma\right) = \left(\frac{\gamma + \left(\frac{d}{D}\right)^2 - 1}{\gamma}\right)^{\frac{\alpha}{2}} + \left(\frac{\gamma}{\gamma + \left(\frac{d}{D}\right)^2 - 1}\right)^{-\frac{\alpha}{2}} - 2 \tag{9}$$

Both the function f and the parameter γ are sub-computations that facilitate the derivation and computations of the integral and do not have any significant physical meaning (for detailed explanations, please refer to [14]).

The kinematic model of the waterjet needle steering is a discrete adaptation of the Bicycle model presented in [181]. Figure 10 depicts the nonlinear kinematic model of needle steering. In this case, $\delta\theta$, $\delta\ell$ and r are the incremental needle

rotation angle, incremental insertion distance and radius of curvature. $\delta\ell$ is equal to the depth of cut (h) of the waterjet in each step, and if the number of steps is n, then the whole insertion length is $\ell = \delta\ell \times n$. To change the needle's direction to reorient the x–y plane in any given step, $\delta\theta$ should be applied to rotate the needle at its base and thus reorient the nozzle at the tip. In this model, the pose of the needle is described by the needle tip frame pose with respect to a reference frame. The needle has a position of $\mathbf{p}_k$ and rotation $\mathbf{R}_k$ at time k. Rotation of $\delta\theta$ about the z-axis gives the rotated tip frame $\mathbf{R}_k' = \mathbf{R}_k \mathbf{R}_z(\delta\theta)$. The position of the needle tip after insertion of $\delta\ell$ can be calculated from the geometry of the circular path as:

$$\mathbf{p}_{k+1}^{k'} = \begin{bmatrix} 0 \\ r(1 - \cos(\Phi)) \\ r\sin(\Phi) \end{bmatrix}, \tag{10}$$

where $\Phi = \frac{\delta\ell}{r}$. The position of the needle tip at time $k+1$, can be found by transforming this vector into the world frame:

$$\mathbf{p}_{k+1} = \mathbf{R}_k \mathbf{R}_z(\delta\theta)\mathbf{p}_{k+1}^{k'} + \mathbf{p}_k \tag{11}$$

Tip orientation at time $k + 1$ can be calculated by:

$$\mathbf{R}_{k+1} = \mathbf{R}_k \mathbf{R}_z(\delta\theta)\mathbf{R}_x(-\Phi) \tag{12}$$

Note that:

$$\mathbf{R}_0 = \mathbf{R}_x(-\beta) = \begin{bmatrix} 1 & 0 & 0 \\ 0 & \cos(\beta) & \sin(\beta) \\ 0 & -\sin(\beta) & \cos(\beta) \end{bmatrix}, \tag{13}$$

where $\mathbf{R}_0$ is the rotation matrix around the x-axis by a deflection angle of $-\beta$.

Kinematic modeling is easy to implement and is not computationally expensive. The main disadvantage of kinematic modeling is that the model parameters should be measured through performing preliminary experiments in the tissues. This is not feasible in practice for actual surgical operations, and therefore the online estimation of the needle trajectory using methods based on Kalman filter is necessary [117]. Kinematic models also do not consider the interaction between the needle's shaft and the surrounding tissue. It is assumed that the shaft of the needle follows the tip trajectory. This assumption is valid when the needle is very flexible, and the tissues are stiff so that the bending forces of the needle are small enough to cause little tissue motions. These assumptions are difficult to provide in actual clinical operations where there are patient motions and variable inhomogeneous tissues.
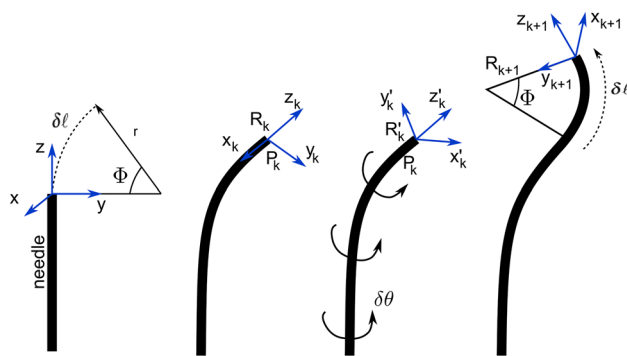
Fig. 10 The kinematic model of the waterjet needle steering. The z-axis is assumed to be tangent to the needle at the tip, and the y-axis is toward the center of the curvature. The needle follows a path in the y–z plane with radius r and arc length ℓ. The frame advances as the needle tip progresses during waterjet needle steering. $\delta\theta$, $\delta\ell$ and r are the incremental needle rotation angle, incremental insertion distance and radius of curvature, respectively. Note that, $\delta\ell$ equals h (depth of cut)

### 2.2.2 Finite element models

Finite element modeling (FEM) is used to model the needle's interactions with the surrounding tissue [127,164]. FEM needs geometry and some physical parameters of the tissues and the needle. A 1D beam model is often used for modeling the needle. A rigid beam [37], a flexible beam [38], and a succession of rigid beams linked by angular springs [57,60] are used to model the needle in the literature.

3D models of the needle are also proposed in the literature [113,188] to efficiently represent the needle's deformations and the effect of the tip geometry. Tissues are modeled with 2D rectangular mesh with elastostatic behavior [38], 3D mesh with real organ shape [31], and dynamic nonlinear behavior [163]. The needle-tissue interaction can be modeled by adding interaction forces due to the lateral displacements of the needle and tangential forces like friction and stiction along the needle shaft [44]. Konh et al. [81] proposed a Finite Element Model to predict the 2D and 3D paths of an active needle with multiple Shape Memory Alloy (SMA) actuators.

The computational complexity of FEM is high in comparison to the other modeling approaches. The time needed for computation is directly related to the model's detailed levels (number of the elements) and the number and complexity of the factors considered. Finding exact boundary conditions and properties of the actual biological tissues are also challenging. Because of these limitations, FEM in real-time is difficult to use [9,61].

2.2.3 Mechanics-based models

To model the needle's entire shaft and its interactions with surrounding soft tissue, mechanical-based models are used.
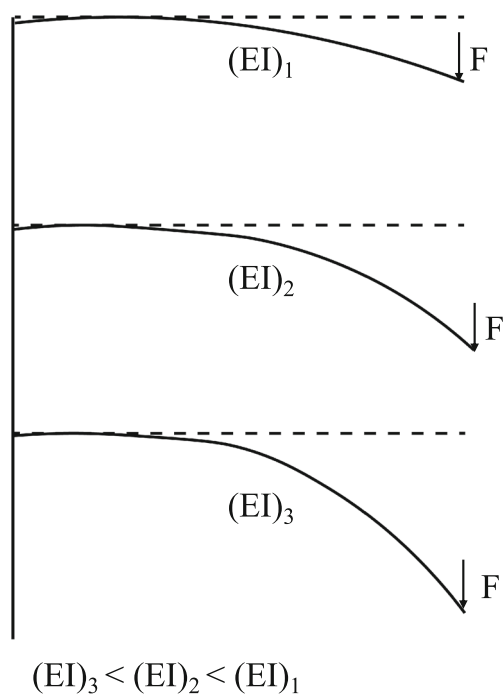
Fig. 11 Bending stiffness of a flexible needle. Under the same loading conditions (for instance, forces from the surrounding tissue), the needle with less bending stiffness deflects more

Fig. 12 Mechanics-based models for needle-tissue interaction using virtual springs (Down) and a continuous load (Up)
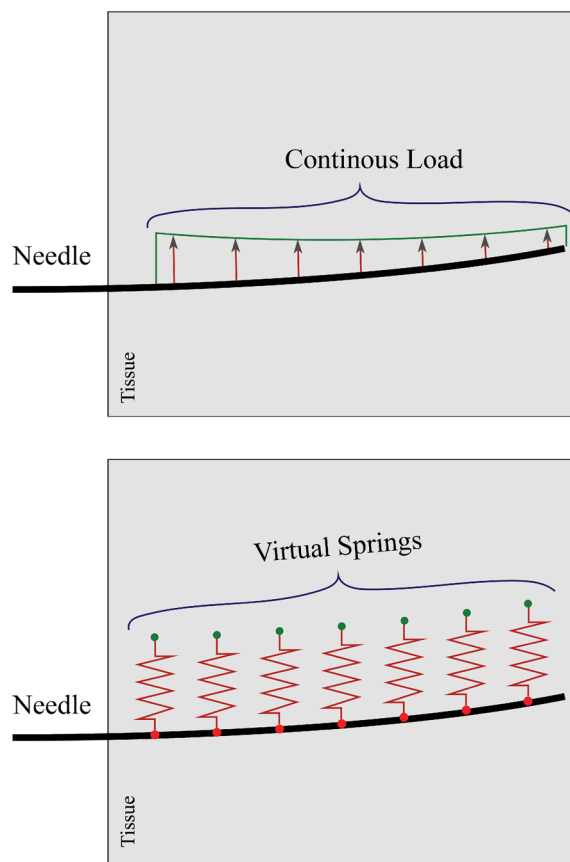
The needle is usually modeled as a 1D beam with mechanical properties of the actual needle. The tissues are not modeled entirely (as is done in FEM), but the local interaction with the needle is considered.

The first method to model the needle-tissue interaction is using Bernoulli beam equations. A set of discrete virtual springs is used along the needle's shaft, which is cut into multiple flexible beams. This is done in 2D by Glozman et al. [56]. This is depicted in Fig. 12, down. Bernoulli beam equations for small deflections are used to compute the shape of the needle, considering that the pose of the needle base and the springs' position are known. The Euler–Bernoulli equation that relates the needle' deflection (δ) to the applied load (f_i) can be expressed as follows:

$$\frac{\mathrm{d}^2}{\mathrm{d}x^2}\left(EI\frac{\mathrm{d}^2\delta}{\mathrm{d}x^2}\right) = f_i \tag{14}$$

where x and EI are position, and flexural rigidity of the needle, respectively. This principle is used by Glozman et al. [56]. Under the same loading conditions on the needle, the needle with less flexural rigidity will deflect more. This is shown in Fig. 11. Flexural stiffness for a needle with Young's modulus of E_n, and radius of r_n is defined as follows:

$$(EI)_{\mathrm{needle}} = \frac{E_n\pi r_n^{4}}{4} \tag{15}$$

According to this equation, a needle with a lower elastic modulus and lower diameter has smaller bending stiffness and thus more flexible.

The distributed load applied along the needle shaft can be used to model the needle-tissue interaction instead of discrete springs to have a smoother behavior [74]. Bernoulli equations are also applicable here. This is illustrated in Fig. 12, up.

The second method of the mechanics-based modeling approaches is energy-based (also known as the Rayleigh-Ritz method) that can be used instead of directly using the Bernoulli equations to compute the needle shape. Misra et al. [112] used this method to compute the needle's shape minimizing the total energy stored in the system. This energy is the sum of the bending energy stored in the needle, the deformation energy stored in the tissues, and the works due to tissue cutting at the tip and the insertion force at the base.

Roesthuis et al. [138] used a combination of virtual springs along the needle shaft and continuous load at the end of the needle to model the needle-tissue interactions. There are different approaches proposed in the literature to find these continuous loads, such as online estimation proposed in [175]. Goksel et al. [57] modeled the needle as a succession

of rigid rods linked by angular springs to model the needle's compliance.

The third method of mechanics-based modeling is modeling the dynamic behavior. The previous modeling approaches allow for modeling the quasi-static behavior of the needle insertion into soft tissue. The needle insertion's dynamic behavior into soft tissue can be considered by adding a mass to the needle beams, adding viscoelastic properties of the soft tissues, and adding a model of the friction along the needle shaft [72,189]. Torsional friction and needle torsion model is also needed for needle rotation around its axis [162].

2.3 Control approaches used in needle steering

The trajectory planning approaches for passive steerable needles cannot directly be applied to active steerable needles because of the difference in their structure. Motion planning for steerable needles is defined as a method to find a set of controls (such as insertions and base rotations for tip-steerable needles) so that the needle tip reaches the specified target while avoiding obstacles and not violating the workspace constraints.

2.3.1 Control of passive steerable needles

Passive steerable needles are nonholonomic systems that are difficult to control in joint space because they are under-actuated and have unintuitive kinematic constraints. Trajectory and motion planning algorithms consist of the minimization of a suitable cost function. Additional constraints such as obstacle avoidance and minimum path can also be imposed on trajectory planning.

Trajectory planning is challenging with passive steerable needles because the needle's curvature depends on the complex needle-tissue interactions [80,81]. The other reason that trajectory planning is difficult for passive needles with bevel tips or pre-bent tips is that they can only steer in 2D with constant curvature. To vary the radius of curvature, base rotation is needed, which results in the asynchronous angle between the base and the tip rotation due to torsional friction (see Fig. 17). Thus, complicated trajectory planning algorithms are needed for passive steerable needles.

Different image-guided control methods are proposed in the literature to autonomously steer the needles [54,136]. Image-guided control of passive steerable needles guides the needle to the target based on a known target location in 3D [69,102]. These control schemes can provide greater needle dexterity and improved accuracy. However, they usually cannot make necessary compensations when the path errors arise [23].

Reed et al. [136] developed a needle steering system with several path planners and controllers to drive the needle to the desired location. They initially used plastisol artificial tissue simulants made of plastic and softener in the ratio of 4:1, which simulate Young's modulus of the prostate (approximately 60 kPa). Two needles with the inner diameters of 0.37 mm, and 0.58 mm, and bevel angles of 45°, and 40° with 12°, and 37° bend angles with 4 mm, and 12 mm tip lengths are used for the experiments. They obtained radii of curvature of 6 cm and 5.5 cm with the small and large needles, respectively. The velocity of insertion is $0.25\frac{\text{cm}}{\text{s}}$. They also simulated a brachytherapy procedure in ex vivo tissue using this needle.

Duindam et al. [41] discretized the flexible needles' control space and proposed an optimization problem that utilizes a cost function that minimizes the control effort and path length. They planned their needle trajectory while considering a stop-and-turn strategy by alternating between rotation-only steps and insertion-only steps. Hauser et al. [62] used the helical shape of the generated paths while constant insertion and rotation velocities are applied to the needle. Best velocities are chosen based on the helical path that lets the final tip position be the closest to the target. A model predictive control approach is used in which the best-chosen velocities are applied for a short time, and the procedure is repeated until reaching the target.

Park et al. [124] proposed a numeric diffusion-based method for trajectory planning of flexible bevel-tip needles in a 3D environment without obstacles. The path is computed numerically based on this algorithm, and the algorithm does not handle the uncertainty of the response of the needle to insertion or direction change inputs. The tissue is modeled as isotropic. Inverse kinematics that uses probability density information is utilized to create needle tip paths to reach desired targets. This is solely a theoretical work, and the theories are not validated with experiments. The planning problem is formulated as a nonholonomic kinematics problem based on a 3D extension of a unicycle model.

Alterowitz et al. [12] used a stochastic motion roadmap to model the probability of obtaining a given 2D pose of the needle tip starting from another tip position and orientation. Based on the map, an optimal set of control inputs is computed to minimize the probability of hitting obstacles and maximizing reaching the target. Lee et al. [85] used fuzzy logic as a way to deal with uncertainty in control inputs. Glozman and Shoham [55] passed a spline trajectory through three points of the obstacle, needle tip, and the target obtained from fluoroscopic images of the tissue before needle insertion. PID controller was used to direct the needle to the target location, and for a 40 mm insertion, the error was 0.5 mm.

Rapidly exploring random trees (RRT) are used by Xu et al. [187] to find the feasible paths in configuration space. RRT is a probabilistic algorithm that randomly chooses multiple possible control inputs and generates the corresponding output trajectories. Then, the best trajectory is chosen and is applied to the real system. Xu et al. [187] used the kinematic

model of the needle with constant curvature to predict the motion of the needle tip, knowing the insertion and rotation velocities. Because of the constant curvature limitation, the control inputs were constrained to a stop-and-turn strategy. In their method, many trajectories should be generated before reaching a suitable one, and due to being slow, it can only be used for pre-operative planning of the insertion.

The concept of duty cycling control that helped eliminate the requirement of constant curvature for path planning is used in 2D by Bernardes et al. [20], and 3D by [22,129]. RRT is also used in 2D with FEM instead of kinematic models to provide a more accurate pre-planning that also considers the tissue deformations due to needle insertion [127].

Alterovitz et al. [10] developed finite element modeling for planning paths around obstacles in deformable tissue. The planning algorithm is developed for bevel-tip-steerable needles, and the obstacles are considered to be in a 2D plane. The planner compensates for tissue deformations and avoids obstacles. The finite element model computes the soft tissue deformations that consider the effects of the needle tip and frictional forces using a 2D mesh. The planning problem is a constrained nonlinear optimization problem that is minimized locally with a penalty method. The planner is not verified experimentally. This method assumed that the bevel direction could only be set once before the insertion. The method uses a local optimization that will fail to find a globally optimal solution while encountering obstacles.

Alterovitz et al. [11] proposed a motion planning algorithm for bevel-tip-steerable needles based on dynamic programming where the needle's path is not certain because of the uncertainties in tissue properties, needle mechanics, and interaction forces. The algorithm involves a cost function to minimize in order for the needle to reach a target location while avoiding obstacles. The motion planning problem is formulated as a Markov Decision Process (MDP), and infinite-horizon dynamic programming is used to compute an optimal control sequence (insertions and direction changes). Without uncertainty, the needle response to controls (insertion and rotation) is a certain and known constant curvature path. In an uncertain case, the probability distribution of responses to control inputs is considered to be known. In the case of discretization error, the planner may not find a feasible solution. Tissue inhomogeneity that causes uncertainty and noise into the needle tip orientation is considered. No experimental validation is provided.

DiMaio and Salcudean [37,39] developed a model-based trajectory planning approach for passive steerable needles. They formulated a Needle Manipulation Jacobian that used numerical needle insertion models with needle deflection and soft tissue deformation. The Jacobian is the relationship between the needle tip and base velocities. Potential field-based path planning technique is used for target reaching and obstacle avoidance. The insertion experiments are done

in an open-loop fashion. Needle and tissue are modeled using the Finite Element Analysis (FEA) approach. This method is complicated and does not allow for online correction of the targeting error. The inverse kinematics of the needle is solved by iterative numerical computing of the needle's Jacobian. Their work did not consider the tip asymmetry. Due to the computational complexity of FEM, only pre-planning of the needle trajectory was done, and the actual insertion was done in an open-loop. If $\begin{bmatrix} x_t & y_t & \theta_t \end{bmatrix}^T$, and $\begin{bmatrix} x_b & y_b & \theta_b \end{bmatrix}^T$ are tip, and base pose of the needle, then:

$$\begin{bmatrix} \dot{x}_t \\ \dot{y}_t \\ \dot{\theta}_t \end{bmatrix} = J(q) \begin{bmatrix} \dot{x}_b \\ \dot{y}_b \\ \dot{\theta}_b \end{bmatrix} \tag{16}$$

The Jacobian defined as the relationship between the needle base and the tip velocities can be found using the following equation:

$$J = \left[\begin{bmatrix} \frac{\partial x_t}{\partial x_b} & \frac{\partial x_t}{\partial y_b} & \frac{\partial x_t}{\partial \theta_b} \end{bmatrix} \quad \begin{bmatrix} \frac{\partial y_t}{\partial x_b} & \frac{\partial y_t}{\partial y_b} & \frac{\partial y_t}{\partial \theta_b} \end{bmatrix} \quad \begin{bmatrix} \frac{\partial \theta_t}{\partial x_b} & \frac{\partial \theta_t}{\partial y_b} & \frac{\partial \theta_t}{\partial \theta_b} \end{bmatrix} \right]^T \tag{17}$$

Glozamn and Shoham [56] proposed an optimal trajectory planning (defined as the computation of the needle base pose for a given tip trajectory) for passive flexible needle steering. Needle insertion into the soft tissue is modeled using a linear beam supported by virtual springs, and the forward and inverse kinematics of the needle are solved analytically. Simulation and path planning are done in real-time. The experimental tests are demonstrated in 2D space. Figure 12, down depicts the proposed virtual springs model for flexible needle insertion into the soft tissue. The tissue's reaction on the needle is modeled using virtual springs distributed over the length of the needle and friction force tangent to the needle shaft. The stiffness coefficients of the virtual springs are found experimentally. They did not model the bevel tip.

Despite the attainable accuracy with autonomous needle steering systems, having the physician in the control loop is desirable from a clinical acceptance point of view of steerable needles. Other than that, passive steerable needles exhibit unpredictable behavior in nonlinear and anisotropic biological tissues.

Romano et al. [140] proposed a teleoperation control scheme in joint space. This control scheme puts the burden of the prediction of the needle's nonholonomic behavior on the user. Majewicz and Okamura [102] proposed Cartesian and joint space teleoperation for nonholonomic steerable needles. The Cartesian space control allows the user to select the robot's desired position in Cartesian space and provides force feedback to represent kinematic constraints and the robot's position error. They showed the efficacy of the proposed control through simulations and not real experiments.

Sun and Altrerovitz [155] considered the sensor placement directly during the design of the planning and LQG controller to minimize the uncertainty on the tip location along the planned trajectory. In that way, the obstacles are avoided without the need to pass far away from them to avoid a collision. Online replanning of the trajectory, which is regularly computing a new trajectory based on the current state of insertion, can also be utilized instead of taking the model's uncertainties into account. This method is used by Bernardes et al. [21], and Patil et al. [128]. Online replanning is only possible if simplified kinematic models are used, and they are not possible with FEM.

Sliding mode control can be used to control the bevel-tip-steerable needles. The advantage of such a control method is that it does not depend on an interaction model's parameters. Rucker et al. [143] used this method and showed that by selecting a suitable ratio between insertion and rotation velocities, accuracy could be reached. Different feedback modalities are used successfully with sliding mode control such as electromagnetic (EM) tracker [143], fiber Bragg grating (FBG) sensors [3,153], ultrasound (US) imaging [1,47], and computerized tomography (CT)-scan with EM tracking [152].

Visual servoing is a control approach based on visual feedback. Krupa [84], and Chatelain et al. [29] used visual servoing with 3D US imaging and the duty cycling method to control the needle trajectory. This method can compensate for modeling errors because the control is directly defined in the image.

Figure 13 shows an example schematic of the image-guided robotic needle steering control and estimation-based control.

2.3.2 Control of active steerable needles

Active steerable needles are controlled with direct dynamic control of needle deflection without the need for complex robotic path planning [23]. Active steerable needles provide controllable actuation from the proximal end, and this gives the physicians real-time manipulation of the needle tip for quick reorientation utilizing image feedback. Common imaging systems include Ultrasound (US), Computed Tomography (CT), and Magnetic Resonance Imaging (MRI).

Lyons et al. [99] used a cost function that depends on the tubular environment geometry to plan trajectories for the active cannula used in lung biopsy procedures. Black et al. [23] proposed an active needle with Shape Memory Alloy (SMA) compatible with MRI guidance. Ayvali et al. [13] used a kinematic approach for trajectory planning for the active cannula.

They proposed an approach to find a minimum path between the desired and final configurations in an obstacle-free environment. They used 6 markers along the shaft of

the needle to find the cannula's pose and a stereo system for stereo imaging. The 3D locations of the markers are found by triangulating the 2D location of the markers on the left and right images. Two PWM-based controllers for SMA actuators are proposed. One is a PWM-based vision feedback controller, and the other is a temperature-based feedback controller.

Overall, a position control with stereo vision feedback is used to control the cannula. The ultimate control goal is to combine the temperature feedback controller with the image-guided position control so that the controller can shift to the temperature feedback controller the image feedback is not optimal. In the vision-based feedback controller, a proportional controller is used to correct the error between the desired angle and the current angle by adjusting the heating time of the SMA wire:

$$t_i = k(\alpha_{\text{desired}}^i - \alpha_{\text{current}}^i), \tag{18}$$

where $\alpha_{\text{desired}}^i$ and $\alpha_{\text{current}}^i$ are the desired bending angle for the ith joint and current joint angle for the ith joint, respectively. The position error is calculated using the stereo image couples.

Van de Berg et al. [167] studied the ability of the human operator to manually correct for errors in the needle insertion path. They used an active, tip-articulated steerable needle with OD of 1.32 mm with a flexure joint near the tip with a retractable stylet. Bending stiffness is in the order of a 20-gauge hypodermic needle. They achieved a targeting error of 0.5 mm ±1.1 during manual steering of the needle under image guidance to 5 different targets. 4 wt%, 8 wt% Gelatin tissue simulants are used to do the steering experiments. Moreover, Van den Burg et al. [169] proposed a linear-quadratic Gaussian (LQG) controller for the needle to robustly follow the preplanned trajectory using RRT. The controller can compensate for the current state uncertainty to minimize the probability of hitting an obstacle.

2.3.3 Sensing modalities in robotic needle steering

Needle steering robotic systems should monitor the state of the insertion to guide the needle accurately. Different feedback modalities are used in the literature to provide different information about the needle and the tissue. Different feedback modalities include Shape feedback, Real-time imaging techniques, and force feedback.

Fiber Bragg Grating (FBG) sensors are used to reconstruct the needle's shape in the literature [40,123]. They consist of several optic fibers integrated into the needle, and depending on the curvature of the fiber at a certain location, the light propagation varies, allowing the measurement of the needle's curvature and retrieving the needle's shape [40,90,123]. Integrating these fibers into the needle makes the needle's design

Fig. 13 (Up) Example of closed-loop control of image-guided needle steering. The steering controller provides needle rotation and curvature needed to reach the target. The robot controller included motor controllers and commanded motor control hardware to move the needle tip along the target's desired path. The imaging system provides visual feedback for the measurement of the tip pose. (Down) Example of an estimation scheme for closed-loop control of image-guided needle steering. The estimation scheme's output is given to the steering controller, which identifies the needle rotation and curvature necessary to reach a target point. An estimation scheme is necessary when the outputs of the imaging feedback are noisy. Kalman filter is a common estimator used in the literature [5]
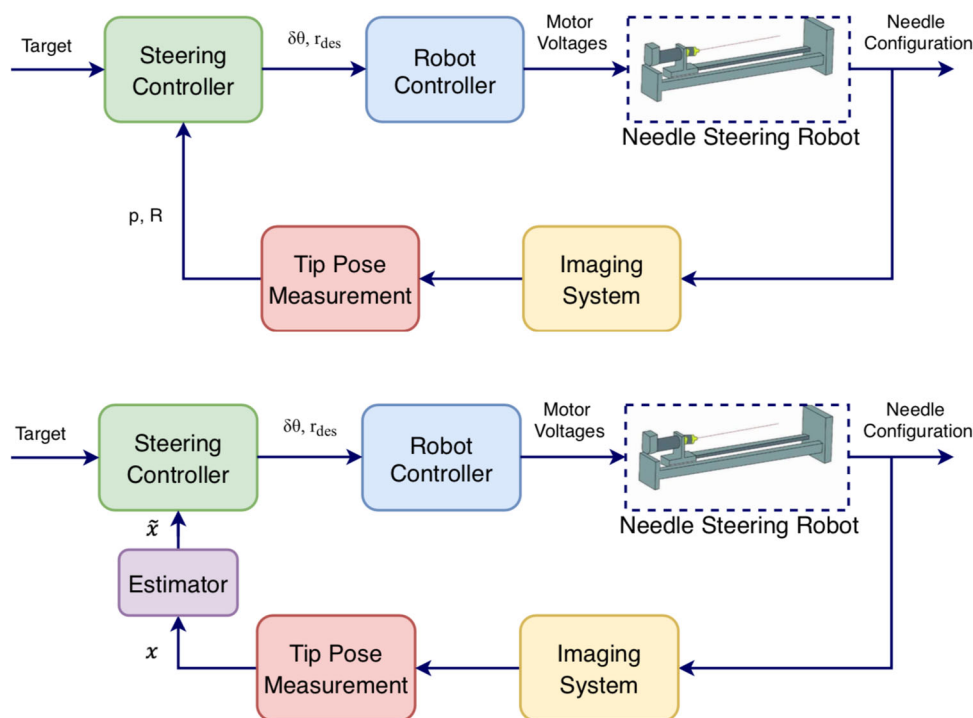
more complicated since the fibers should follow the same deformations of the needle.

Electromagnetic (EM) trackers are usually used to track the needle's tip's pose (position and orientation). Currently, some miniaturized trackers can be embedded in standard needles.

The above-mentioned sensors provide information about the needle position, and to know the target location, different imaging modalities should be used. Imaging techniques can provide feedback both on the position of the needle tip and the target region. Ultrasound (US) is the most common imaging modality since it has a fast acquisition rate of 2D, 3D images, good resolution, and safety. The limitation of ultrasound imaging is the low quality of the images.

Computerized Tomography (CT)-scan and Magnetic Resonance Imaging (MRI) are other commonly used imaging techniques. Unlike the US, they provide high-quality images and a large field of view. However, their limitation for real-time image-guided robotic needle insertion is long acquisition time, and they cannot be used in real-time. Another option for real-time imaging is CT-fluoroscopy. The limitation is that it can expose the physician to a high dose of harmful radiation. Using them in teleoperated robotic needle insertion systems also exposes the patient to radiations that are unnecessary for real-time procedures. Patel et al. [126] used a fast MRI acquisition system for image-guided needle insertion. They have acquired a 2D image every 750 ms by reducing the image size and quality.

Force sensors are used in the literature to measure the forces applied to the needle and the tissue. Force sensing is useful to evaluate the needle performance while puncturing through different tissue layers [121]. Force sensing is also used with teleoperated robotic systems to provide the physician or compensate for tissue motion [68,130].

2.4 Clinical acceptance of steerable needles

Several limitations of needle steering have hindered the widespread clinical use of steerable needles to date. These limitations are buckling and compression of the shaft, excessive tissue damage because of needle base rotation, the difficulty of control due to torsional effects on the shaft and needle deflection at tissue boundaries (needle deflects from its desired path while puncturing a tissue interface), and limited workspace because of the restricted radius of curvature [133,134,159,161,162,178]. There are also several limitations associated with the magnetically steered catheters and continuum manipulators such as limited curvature and buckling.

Compression effects such as buckling of the needle shaft and torsional effects in the shaft cause unnecessary damage in the tissue, inaccuracies in control, and increased model complexity. Buckling can occur when the needle tip faces a tissue that it cannot penetrate or due to collision and inhomogeneity in the tissue [118]. This can be solved if the elastic shaft is not load-bearing. The fact that the shaft should be strong enough to withstand the compression stress contradicts the fact that

it should be flexible enough to allow steering. Eliminating this conflict can show the potential to reduce restrictions on achievable ROC caused by load-bearing shafts.

Torsion in the needle shaft can be caused by the friction between the needle shaft and the tissue. Torsional effects can cause the base and the tip to rotate out of sync. Differences between the base and tip rotations as high as 45 degrees for needle insertions of only 10 cm are reported in the literature [133,135]. It can also cause difficulty in modeling and control [161,162]. Another necessity for clinical acceptance is the steerable needle's ability to follow complex trajectories and maneuver in all three dimensions (3D).

Almost no steerable needle was used on a patient as one of the needle steering system's main components (see Fig. 14). However, some research in the literature demonstrates the use of steerable needles in the clinical environment. Majewicz et al. [103] showed that an enlarged prostate cannot be reached with a straight needle insertion due to pubic bone and suggested pubic arch interference (PAI).

Webster et al. [181] proposed that robotic needle steering can be used to treat hepatocellular cancer using thermal ablation. Systems are proposed in the literature [9,36,67,100] for brachytherapy of prostate cancer. Needle steering is useful for compensation of needle deflection, tissue deformation, and target dislocation during needle insertion. Needle steering scenarios are also designed to emulate environments for neurosurgery [46,51] in which deep tumors can be difficult to reach by straight needle insertions. Figure 14 shows a schematic of clinically viable steerable needle.

Majewicz et al. [101] evaluated the performance of tip-steerable needles in inhomogeneous soft tissues in terms of the radius of curvature and insertion forces. They concluded that steerable needles curved more in the kidney than in the liver and prostate because of the tissue properties differences. Higher insertion forces in the liver were observed with pre-bent needles, and they exhibited more curvature in vivo than ex vivo. The minimum radius of curvature of 5.23 cm is achieved with pre-bent needles in ex vivo tissue and 10.4 cm in in vivo tissue. Bevel-tip needles achieved negligible curvature for in vivo tissue and a minimum radius of curvature of 16.4 cm in ex vivo tissue.

They only showed the feasibility of clinical application for needle steering through targeting and ablating cadaveric canine liver. The needle diameter for insertions into the liver and the prostate is 0.74 mm, and for the kidney, it is 0.58 mm. Bevel-tip needles had a bevel angle of 30°, and pre-bent tip-steerable needles had a 15° pre-bent tip angle with 30° bevel angle. Needles are made of Nitinol wires. Insertion speed for needle insertions is $0.5\frac{\text{cm}}{\text{s}}$. Mean insertion force was measured to be $1 < F_{\text{insertion}} < 2$ for bevel, and bent tips in ex vivo prostate, kidney, and liver, and $0 < F < 1$ for insertions into in vivo prostate, kidney, and liver using bevel and pre-bent needles.

Constant curvature steerable cannula is used by Burgner et al. [25] to debulk the simulated clot in the brain phantom to show an application of steerable needles in neurosurgery. The cannula's tip is controlled by insertion, retraction, and axial rotation of the cannula under image guidance. In vitro experiments showed the feasibility of evacuating 83–92% of hemorrhage volume.

3 Discussion

Needle steering systems came into existence intending to improve percutaneous interventions. Using a superelastic needle that can follow curved trajectories, the needle can be steered around anatomical obstructions to a target area (lesion or tumor). This can reduce trauma to the patient to a great deal. This potential has drawn a significant research interest in this direction.

In most needle steering methods proposed in the literature, the curvature is created using an asymmetric force at the needle tip that changes the direction of tissue fracture. Traditionally, this has been accomplished through beveled tips or pre-curved sections near the end of the needle. These asymmetric forces between the needle tip and the tissue cause the deflection of the needle (see Fig. 15).

Because of the radial component of the force acting on the tip, the needle moves sideways. Orientation of the tip is controlled by rotation at the base (see Fig. 16). The radius of curvature can be controlled for a given tissue/needle combination using complex methods such as manipulating the tissue via external forces and duty cycling (continual spinning of the needle at the base). Note that the needle curvature can only be decreased with duty cycling, and the maximum curvature can only be achieved through 0% duty cycling.

The mechanism at the tip that results in this asymmetric force can take on a variety of design paradigms: beveled, complex, active, inactive, programmable, composite, and articulated. Conventional steerable needles have large radii of curvature, especially in very soft tissues, because the tissue's stiffness is too low to apply forces large enough to curve the traditional needles, and the needle tends to move in straight paths. The steerability of a steerable needle is defined as the minimum achievable radius of curvature, which is the reciprocal of the needle circular path's curvature. Large radii of curvatures restrict the reachable workspace, showing the importance of achieving smaller radii of curvature by proposing new and effective methods.

Bevel-tipped needles made of superelastic materials (mostly Nitinol) dominate the needle steering literature. The similarity in design to conventional clinical needles and ease of manufacture made them an attractive alternative to these needles. Several researchers tried to tweak the bevel-tipped needles to overcome their limitations. From there, pre-

Fig. 14 Clinically viable steerable needle system. Clinical trials with real patients have been one of the main components missing in the needle steering research to date
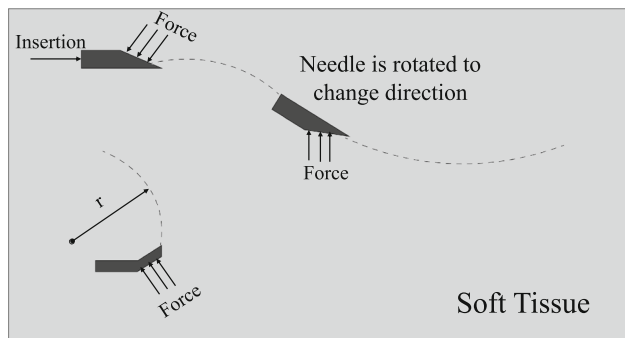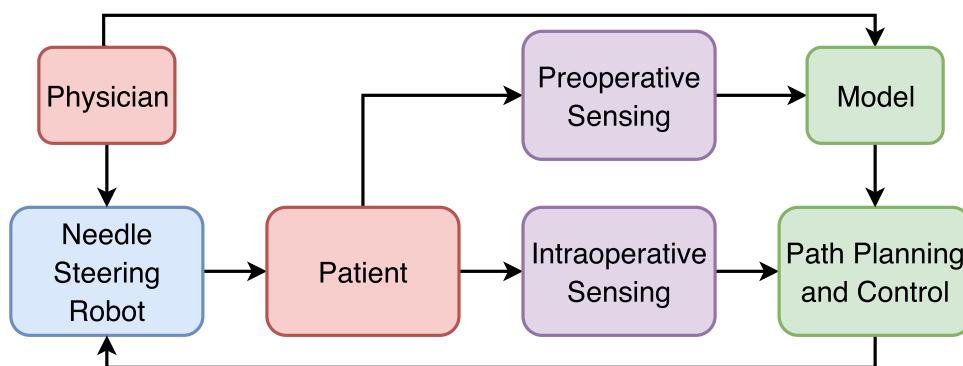
Fig. 15 Principle of steering in conventional steerable needles. Tip-steerable needles rely on interaction forces from the soft tissue to be able to steer

Fig. 17 The effect of torsional windup and torsional friction when rotating a long flexible needle. Torsional friction and rotational inertial effects cause the tip angle to be out of sync with the base angle due to the rotational dynamics along the length of the needle

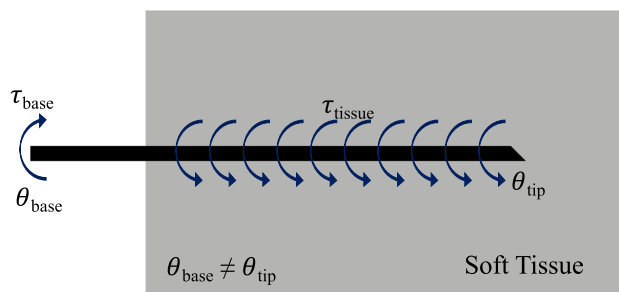**Fig. 16** Tip-based needle steering concept. Steerable needles can steer around obstacles and reach multiple targets from one insertion unreachable by straight needles. Anatomical obstacles can be veins, bones, nerves, and other structures that a needle cannot penetrate or cause unwanted consequences. Steering direction can be changed by rotating the needle at the base

curved, pre-bent [132], "airfoil" tip [45], articulated tip [7], and flexure tip [159] steerable needles came into existence.

Bevel-tip needles rely on the asymmetric force interaction between the surface area of the bevel tip and the tissue to steer. Steering in 3D requires the bevel tip's reorientation through spinning around its axis, and straight insertion needs continuous rotation while being pushed forward. Furthermore, rotating a flexible long needle inside the soft tissue generates

torsional friction on the needle body that leads to a difference in orientation of the needle tip and the needle body that causes loss of control over the needle path [134,136,147,161,162] (see Fig. 17). Continuous rotation can also cause spiral track in the soft tissue that increases tissue damage [19,107].

Especially for pre-bent, and pre-curved designs, duty cycling causes significant tissue damage [159]. Pre-bent needles also do not have direct control over the needle curvature, and the only way to correct it is to retract the stylet, rotate it, and re-insert it. This increases the time of procedure and damage to the tissue [134]. Therefore, the remaining challenges of conventional steerable needles to be solved are needle steering with less damage to surrounding tissues, decreasing the minimum radius of curvature for better steerability and controllability, especially in very soft tissues such as the brain and liver, and varying the curvature in a more efficient way than duty cycling.

It is also proven that the needles with diameters less than 1 mm reduce the risk of complication and patient's discomfort [147]. Decreasing needle diameter decreases the second moment of inertia, which lowers the bending stiffness of the needle and thus increases flexibility and steerability [146]. Thus, it seems that proposing steerable needles with submillimeter diameters to decrease patient trauma and increase needle curvature is necessary.

Table 1 Soft tissue-mimicking materials used in the literature and their preparation methods

Soft tissue simulant	Preparation method
SEBS phantoms	SEBS polymer in mineral oil
	heated to 120 °C to dissolve
	while stirring
	Allow to cool down to room temperature
Polyvinyl Alcohol (PVA) gels	PVA powder plus deionized water
	and heated up to 93 °C
	while magnetically stirring
	Allow to cool down to room temp
Polyvinyl chloride (PVC) Plastisol	PVC resin in liquid plasticizer
	then heating to (170–190 °C)
	while stirring.
	Allow to cool down
Gelatin gels	Gelatin powder with deionized water
	Heat to dissolve. For cooling refrigerate
	at 4–8 °C
Agar/Agarose gels	Agar in the gel form:
	heated until becoming liquid and
	then cooled and refrigerated overnight
	Agarose is a solution of 4% agarose powder
	in distilled or deionized water
	while magnetically stirring. Then cooling
Silicone gels	A mixture of polyorganosiloxanes (65–85 wt%),
	amorphous silica (20–25%), platinum-siloxane
	complex (0.1 wt%), and some other ingredients (10 wt%)
	Vaseline oil is added to improve acoustic properties
	Mineral oil is used to adjust the mechanical properties

PVA is non-toxic, hydrophilic, and biocompatible. Properties can be controlled by varying the ratio of the additive materials or changing the cross-linking method. PVA, PVC, gelatin, and Agar phantoms are water-based. SEBS phantoms are oil-based

Without local actuation, the minimum radius of curvature obtained with the steerable needles is limited, limiting the steerability. In the case of tissue inhomogeneity, crossing tissue boundaries, or going through one tissue to the other, the needle deflects from its preplanned trajectory. Developing needles that can exert localized forces to correct errors in trajectory instead of dependency on the needle and soft tissue interaction forces for steering is a possible solution.

Active-type steerable needles came into existence in recent years to solve this issue. These designs lack the proper modeling and control developed for them. Programmable bevel [79,177], tendon-actuated steerable needles [166] (embedding tendons in the steerable needle design increases the thickness of the needle), and Shape memory alloy (SMA) steerable needles [81,83] are some of the proposed designs in the literature. The programmable bevel steerable needle proposed by Ko et al. [79] is inspired by the ovipositor of the wood wasp and can achieve variable curvatures. The proposed needle is too thick (12 mm) because of its special design. Moreover, using SMA for Needle steering is promising; however, there are currently size limitations for it and are not suitable for thin needle manipulation and navigation.

Recent research trends show a considerable effort on the control strategies for steerable needles [108,116,166]. Control strategies and motion planners are developed for solving the control problem for dynamic environments with uncertainties. Adaptive controllers [117,143] in which parameters can be estimated and updated online offer a potential advantage to steerable needles since the system does not need to go through pre-operation calibration through prior insertions and are best for regions that tissue mechanical properties change. Online adaptive path planning became more and more frequent in recent years. Pre-operative planners are computationally expensive since they should find an optimal path based on the surgeon's input. Moreover, they need the behavior of the soft tissue beforehand to find the best possible trajectory. Online planners can solve these limitations by adapting to changing environments or uncertainties. They

Table 2 Soft tissue simulants and soft tissues that they simulate in terms of mechanical properties

Soft tissue simulant composition	Needle insertion peak force (N)	Elastic modulus (kPa)	Soft tissue	References
SEBS 10% in mineral oil	–	42.5	Uterus, and cervix	[15,16]
SEBS 15% in mineral oil	–	112.9	Muscle	[14,18]
PVA hydrogel 1	–	–	Human vitreous	[95]
PVA hydrogel 2	5.3	11.4	porcine liver	[65]
PVA hydrogel 3	8.05	–	prostate	[91]
PVA hydrogel 4	–	1–2	Brain	[50,173]
PVA hydrogel 5	0.23 ± 0.04	116	Kidney	[66]
PVA hydrogel 6	–	9.44	brain white matter	[111]
PVA hydrogel 7	0.11–0.16	–	Liver	[35]
Gelatin gel 1	–	0.997–50.71	Layers of skin	[30]
PVC gel 1	5.2	3–200	Prostate	[63]
PVC gel 2	0.04–0.36	6–45	Liver	[92,93]
Silicone with 20, 30, and 40 wt% mineral oil	0.4–1	10.3–13	Liver and muscle	[176]
Gelatin 3.4 wt%	–	3–4.5	Brain	[88]
Gelatin 15 wt%	–	10	Liver	[166]
Gelatin 14.9 wt%	–	35	Breast	[139]
1.3 cc of Gelatin in 20 cc of water	Comparable insertion force	–	Brain	[110]
Gelatin 5 wt%	–	4.6	Brain	[48]
Gelatin 10 wt%	–	25	Normal fat tissue	[116]
Gelatin 20 wt%	–	90	Cancerous prostate	[116]

PVA hydrogel 1: PVA hydrogel with Sodium trimetaphosphate (STMP) additive in the ratio of 8:1. PVA hydrogel 2: PVA hydrogel with Dimethyl-sulfoxide (DMSO) additive (3 wt% PVA + DMSO + deionized water). PVA hydrogel 3: PVA hydrogel with 3 g PVA + 17 g deionized water + 90 g DMSO + 4 g NaCl + 1.5 g NaOH + 3 g ECH. PVA hydrogel 4: 6% PVA and phytagel (PHY) 0.85% separate solutions in 1:1 weight ratio. PVA hydrogel 5: PVA concentration of 8 g/dl with 4$wt\%$ NaCl concentration with mix water/DMSO solvent prepared under 7 freeze/thaw cycles. PVA hydrogel 6: (PVA + Polyvinyl pyrrolidone(PVP)) polymers are mixed with deionized water at a concentration of 10 wt% heated to 85° C for 3 h. PVA hydrogel 7: 4$m\%$ PVA with 2 freeze/thaw cycles. Gelatin gel 1: gelatin powder + agar powder dissolved in distilled water (different concentrations for different layers) + (synthetic melanin powder + Intralipid-20% + molecular absorbing dyes + India ink) for optical properties + (bovine serum albumin (BSA) + 40 μm diameter monodisperse silica microspheres) for acoustic properties. PVC gel 1: PVC polymer solution and the softener diethyl hexyl adipate (different concentrations). PVC gel 2: PVC polymer solution and the softener diethyl hexyl adipate (soft PVC)

seem to be essential in case of the target location changes during the course of operation.

Robotic needle steering has now been a research discipline for over a decade, yet the progress toward clinical testing and implementation has been slow. It is believed that much of the slow adoption of steerable needles for real clinical applications has been caused by the poor curvature performance of many of the needle strategies in biologically relevant tissue stiffnesses. Only one case of in vivo studies is reported by Majewicz et al. [101] that did some open-loop curvature measurements and did not simulate a real clinical scenario.

Most of the needle steering techniques are validated in artificial tissues rather than actual biological tissues, and most of them have minimal curvature in soft tissues. Soft tissue phantoms made of Gelatin are very common. According to literature, Gelatin 5 wt.% phantoms have stiffnesses of 4.6 kPa which correspond to the stiffness of brain tissue (0.5–6 kPa) [48]. Gelatin 10% and 20% soft tissue phantoms have Young's moduli of 25 kPa, and 90 kPa, respectively, and can simulate normal fat tissue (E 22 kPa) and a cancerous prostate ($E \approx 96$ kPa) [116]. 6% by weight gelatin soft tissue phantoms is reported to simulate the in vitro canine brain's resistance at 38° C [78,137]. From compression tests conducted in [34], it is found that the elastic moduli of the 5% and 7% by weight gelatin phantoms are 21 kPa, and 80 kPa, respectively (note that the elastic moduli reported by different literature differ significantly).

Despite the vast research in the needle steering area, this research is still immature for clinical settings. However, almost all the needle steering experiments are conducted in soft tissue phantoms such as gelatin and agar [112], or ex vivo tissue samples [104]. One in vivo study is reported in the literature that is carried out on canine prostate, liver, and kidneys [101]. This is the only in vivo study reported in the literature. This suggests that there are still fundamental issues to be solved before clinical adoption of this technology. One limitation is the complex closed-loop control of the steerable needles that make their application in clinical settings challenging. For example, it is a big challenge to change the control parameters in real-time as the local tissue mechanical properties change. Another unsolved challenge is the registration of the needle and the local tissue environment to avoid large placement errors.

Most of the needle steering systems are controlled autonomously with the human operator to set up the system and monitor it during operation. However, for clinical acceptance, human-in-the-loop control is needed. Adopting a clinically acceptable placement error for needle steering procedures is challenging. Successful procedures depend on how effective the therapy was (in brachytherapy, for instance, this translates into the radioactive seeds' accurate placement). Typical misplacement errors are reported to be approximately 4 mm in the literature for brachytherapy [97,172]; however,

Table 3 Optical and acoustical properties of soft tissue-mimicking materials and their real soft tissue counterparts that share similar properties

Soft tissue simulant	Absorption coefficient (cm⁻¹)	Reduced scattering coefficient (cm⁻¹)	Speed of sound (m/s)	Attenuation coefficient (dB/cm)	Soft tissue	References
PVC 1	0.1–0.6	5.9–16.2	1499	6.2–22.7	Breast	[171]
PVC 2	–	–	1360–1400	–	Prostate	[63]
PVC 3	0.4–2.8	0.1–2.8	1403–1409	0.5–0.69	Liver, fat	[49]
PVC 4	–	–	1379.3–1397.9	0.29–0.94	Breast, and lesions	[33]
Soft PVC plastisol	–	–	1395	0.441	Fat, muscle, liver	[28]
PVC 5	–	–	1393–1407	0.38–0.61	In, fat, muscle, prostate	[93]
Agar 1	–	–	1050	0.08	Skin, breast	[191]
Oil + Gelatin + Agar	–	–	1490–1570	0.1–0.9	breast tissue: glandular tissue, adipose tissue, skin, and Cooper's ligaments	[27]
PVA + water + DMSO	–	–	1570	0.58	Skin, breast	[191]
Silicone 1	–	–	1030	2.8	Skin, breast	[191]
Silicone 2	–	–	964.7–1250	0.546	Fat, muscle, liver	[28]

These properties are useful for image-guided medical interventions

PVC 1: PVC plastisol with glass microsphere. PVC 2: PVC polymer solution and the softener diethyl hexyl adipate (different concentrations). PVC 3: PVC plastisol (PVC + softener). PVC 4: PVC plastisol mixed with graphite (different concentrations). PVC 5: polymer solution + softener phthalate ester with mineral oil and spherical glass beads (50 μm average diameter). Agar 1: 2% solution agar powder in distilled water heated to 160° C while stirring and then cooling down. Silicone 1: A two-compound silicone (9:1 mass ratio of platinum catalyst:hardener). Silicone 2: Silicone mixed with silicone oil with different ratios

Table 4 Overview of the state of the art in robotic needle steering, design, specifications, Modeling, planning, and clinical applications

Refs.	Needle design	Needle material	Needle diameter (mm)	Insertion velocity (mm/s)	Soft tissue	Best ROC (mm)	Needle localization	Planning	Model	Clinical application
[7]	Passive Articulated tip (45°, 16 mm)	Nitinol	0.8 (body) 2 (hinge) 1 (tip)	1.6	Ex vivo Porcine liver	55.8	3D US	–	Kinematic	Liver Biopsy
[24]	Passive "Airfoil" Bevel tip (12°)	Nitinol	0.46 (cannula) 0.24 (stylet)	3	Gelatin 6% Gelatin 10% Ex vivo Cow Liver	125 72 263	Camera	–	–	–
[75]	Passive 4 sets of Notches	Stainless Steel (SS)	1.02	5	80% liquid plastic + 20% plastic softener $E = 35$ kPa		US Guidance	–	Finite Elements	–
[80]	Passive Bevel tip (30°)	Steel	0.38	2.5	Plastisol (3:1 plastic to softener)	–	–	–	Finite Elements	–
[101]	Passive Bevel tip (30°)	Nitinol	0.58	5	Ex vivo Canine Kidney	164.5	X-ray + Camera	–	–	Brachytherapy Biopsy
[101]	Passive Pre-bent (15°) Bevel tip (30°)	Nitinol	0.58	5	Ex vivo Canine Kidney In vivo Canine Kidney	52.3 104	X-ray + Camera	-	-	Brachytherapy Biopsy
[104]	Passive Pre-bent (45°)	Nitinol	0.58	15	ex vivo Goat Liver	34	X-ray + Camera	–	–	Biopsy
[110]	Passive Pre-bent (15°) Bevel tip (10°)	Nitinol (body) SS (bevel tip)	1.27 (tip) 0.28 (body)	–	Gelatin 6.5 wt% (Brain Phantom)	52	–	–	Kinematic	–
[114]	Passive Bevel tip (38°)	Nitinol	0.4	2.5	Plastisol (4:1 Plastic to softener)	179.4	Camera	–	Mechanics-based	–
[122]	Passive Cannula & Pre-bent stylet	Nitinol	0.902	5	PVA gel ($E = 157$ kPa)	–	–	–	Mechanics-based	Biopsy

Table 4 continued

Refs.	Needle design	Needle material	Needle diameter (mm)	Insertion velocity (mm/s)	Soft tissue	Best ROC (mm)	Needle localization	Planning	Model	Clinical application
[143]	Passive Bevel tip (35°)	Nitinol	0.86	–	Simulated Muscle Ex vivo Bovine Liver	128 400	EM Tracker	Adaptive	Kinematic	–
[159]	Passive Bevel tip (10°) Flexure max. angle (22°)	SS (body) Nitinol (flexure)	OD = 0.91 ID = 0.6	5	Gelatin 10 wt% Ex vivo pork loin	121 176	–	–	–	Bronchoscopy
[128]	Passive Pre-bent Bevel tip	Nitinol	0.88	–	Simulate Muscle Ex vivo Porcine loin	67 137	2.5D US	Simulated Annealing	Vibrating Beam	–
[184]	Passive Flexure needle tip Bevel (10°) Notched wall	Nitinol	0.91	–	Knox Gelatin 10 wt% Ex vivo Bovine liver	91.4 224.11	–	–	–	–
[186]	Passive Bevel tip (7°)	Nitinol	0.52	–	Kidney Phantom	333	–	–	–	–
[37]	Passive Base Manipulation	–	–	–	PVC Phantom $E = 20$ kPa	–	Camera	Inverse Kinematics	Finite Elements	–
[21]	Passive Bevel tip (20°)	Nitinol	0.508	–	Agar + 10% Glycerin	60	Camera	Rapid-RRT	Kinematic	–
[6]	Passive Pre-bent (4.5 mm) Bevel tip (45°)	Nitinol	0.48	–	Ex vivo Bovine liver	51.4	2.5D US Doppler	Kinematic	Kinematic	Liver Biopsy
[2]	Passive Bevel tip (30°)	Nitinol	1	4	Ex vivo Chicken breast embedded in Gelatin	270	2.5D US	Rapid-RRT	Kinematic	–
[124]	–	–	–	–	–	–	MRI	Inverse Kinematics	Kinematic	–
[108]	Passive Pre-bent (3 mm)	Nitinol	0.5	–	Paraffin phantom Ex vivo Pork tenderloin	500 600	3D US	Rapid-RRT	Kinematic	–

Table 4 continued

Refs.	Needle design	Needle material	Needle diameter (mm)	Insertion velocity (mm/s)	Soft tissue	Best ROC (mm)	Needle localization	Planning	Model	Clinical application
	Bevel tip (30°)									
[181]	Passive, Bevel tip (45°)	Nitinol	0.7	5 to 25	Simulated Muscle		Camera	–	Kinematic	–
[132]	Passive, Pre-bent (15°), Bevel tip (45°), Bevel tip (45°)	Nitinol	0.61	–	Plastisol (4:1 Plastic to Softener)	61	Camera	Stochastic Motion Roadmap (SMR)	Kinematic	–
[45]	Passive, "Airfoil", Pre-bent (16°, 6.3 mm), Bevel tip (20°)	Nitinol	0.15	–	Knox Gelatin (20 cc boiling water + 1.3 cc Gelatin)	100	Magnetic Displacement Sensor	–	–	–
[125]	Passive, Bevel tip (45°)	Nitinol	0.57	2.5	Plastisol (4:1 Plastic to Softener)	161.3	Camera	–	Kinematic	–
[183]	Passive, Pre-curved	Nitinol	0.48	1.5	Plastisol (4:1 Plastic to Softener)	15.5	Camera	–	–	–
[86]	Passive, Tube-Pre-bent, Wire type	Nitinol	Wire (0.8 mm), Tube (ID = 1, OD = 1.2)	–	Ballistic Gelatin, Cow liver, Beef	20, 104.5, 18.6	Camera	–	–	–
[54]	Passive, Base Manipulation	SS 22-Gauge	OD = 0.711, ID = 0.394	–	Turkey breast muscle, Beef liver	–	Fluoroscopic feedback	Inverse Kinematics	Virtual Springs	–
[119]	Passive, Base manipulation	SS 20-Gauge, Bevel tip	0.908	–	Two-layer Dermasol, Phantom prepared with TiO2	–	US Guidance	Inverse Kinematics	Virtual Springs	–

Table 4 continued

Refs.	Needle design	Needle material	Needle diameter (mm)	Insertion velocity (mm/s)	Soft tissue	Best ROC (mm)	Needle localization	Planning	Model	Clinical application
[23]	Active Single SMA wire	Flexinol	Variable	–	Prostate Phantom	–	Optical FBG Temperature Sensors	–	–	Percutaneous Surgery Biopsy
[83]	Active Single SMA wire	Nitinol/Flexinol	2.6	2.5	Plastisol (3:1 Plastic to Softener $E = 25.6$ kPa)	–	–	–	–	–
[81]	Active Three SMA wires	Solid base/ Flexinol	OD = 2.6 ID = 1.8	–	air	–	–	–	1D Constitutive Material Model of SMAs	–
[147]	Active Cable actuated Pre-bent (10, 20, and 30°)	Nitinol wires SS Tube	0.5	2	Gelatin 10 wt% ($E = 17$ kPa)	–	Camera	–	–	–
[166]	Active Cable Actuated (4 cables)	SS Stylet PEEK Plastic Cannula	Stylet (0.5) Cannula (0.9) OD = 1	5	Gelatin 15 wt% ($E = 10$ kPa)	181	FBG	PI-controller	–	–
[64]	Active Magnetic	Different Gauge Medical Needles	1.59	0.5	Tissue 1 ($E = 1.96$ kPa) Tissue 2 ($E = 2.7$ kPa)	10.2	Magnetic Sensor	PID	–	–
[32]	Active Flexure based SMA wires	Nitinol (body) SS (tip)	OD = 2.2 ID = 1.7	2.54	Plastisol (3:1 Plastic to Softener) Ex vivo Pig liver	387 267	–	–	–	–
[139]	Active Tendon-driven actuated tip (conical shape, l = 5 mm)	Nitinol (needle) PEEK (cannula)	Needle (1) Cannula (2)	5	Gelatin 14.9 wt% ($E = 35$ kPa)	200	FBG Sensors	Online Estimation	Kinematic	–

Table 4 continued

Refs.	Needle design	Needle material	Needle diameter (mm)	Insertion velocity (mm/s)	Soft tissue	Best ROC (mm)	Needle localization	Planning	Model	Clinical application
[145]	Active SMA-actuated with Symmetric tip	Nitinol/ PTFE	1.67	0.5	Plastisol (4:1 Plastic to Softener $E = 40$ kPa)	–	Optical Fiber Sensing	–	–	Prostate Biopsy
[26]	Active 4 Actuated Shafts	Special Flexible and Rigid materials	8	1	Gelatin 6 wt%	100	EM Sensor	–	–	Neurosurgery
[77]	Active 2-Segment Programmable bevel	VeroWhite	4	0.5	Gelatin 6 wt% ($E = 7$ kPa)	70	EM sensor + Camera	Gradient-based Optimization	Kinematic	Neurosurgery
[13]	Active Segmented cannula Pre-curved SMA wires	Flexinol	ID = 1.4 OD = 3	–	Knox Gelatin	–	OCT imaging	Optical flow Algorithm	Kinematic	–
[79]	Active 4-Segment Programmable bevel	Rubber-like	12	1	Gelatin 6 wt% ($E = 7$ kPa)	178.6	2D US	Inverse Kinematics	Virtual Springs	–
[15]	Passive waterjet nozzle	Nitinol	0.24	1	Gelatin 10 wt% SEBS 10% SEBS 15%	78 82 59	Camera	Genetic Algorithm	Kinematic	–

Tissue 1: 1.2 g agar powder + 0.08 g agarose powder + 100 mL distilled water, Tissue 2: 1.6 g agar powder + 35 μg pure charcoal + 100 mL of distilled water, *US* ultrasound, *EM* electromagnetic, *FBG* Fiber Bragg Grating, *OCT* Optical Coherence Tomography, *ROC* Radius of Curvature. Note that some of the values for Radius of Curvature are extracted from the data in the paper

this can be reduced to 1.8 mm with the proper insertion method.

The vast majority of robotic steerable needles are validated in soft tissue-mimicking phantoms. Phantoms are interesting because they can partially mimic the properties of real tissues and steer clear of the need to test these devices on patients. Although no soft tissue-mimicking phantom can simulate real soft tissue properties, they can provide many advantages that make them appealing to characterize and test different needle insertion modalities. This is also important from a training point of view since most residents and trainees do not have the required licenses to do medical operations on patients. Thus, using soft tissue phantoms can improve their expertise during training.

Soft tissue has several properties that are important for image-guided needle interventions, including microstructure characteristics, mechanical properties, optical properties, and acoustical properties. Based on the application, the soft tissue phantom should mimic one or more of these characteristics. Table 1 summarizes the soft tissue phantoms in the literature along with their preparation methods. Table 2 summarizes different compositions of the soft tissue-mimicking materials and the soft tissue they simulate in terms of mechanical properties. Note a variation in the data among different literature. Table 3 provides information on the optical and acoustical properties of soft tissue-mimicking materials and their soft tissue counterparts. This information is useful for image-guided medical interventions.

An overview of the robotic needle steering systems and their design, modeling, planning, and clinical applications that are discussed so far is summarized in Table 4. As can be seen from this table, most of the literature is prevalent with tip-steerable needles in which the interaction of the needle tip with surrounding tissue causes the needle to steer. The curvature is constant and can only be controlled by duty cycling to worsen the radius of curvature. There exists only one radius of curvature for a combination of tissue and the needle. Active steerable needles have some form of control on the needle tip and can steer in 3D without the need for base rotation. However, because of the design complexity, they have larger diameters.

4 Conclusions

In this paper, the state of the art in robotic needle steering, including design, modeling, path planning, and control, is presented, and the advantages and disadvantages of the proposed approaches are discussed. This review has also identified many of the limitations of previously existing steerable needle designs and some of the potential reasons why robotic needle steering has not gained much clinical acceptance.

Robotic needle steering came into existence with the promise of improving medical interventions. However, the clinical acceptance of steerable needles is hindered by the limitations of the traditional steerable needles. The most salient limitations in previously existing designs have been buckling, torsional windup, and a limited workspace. This limited workspace is most affected by the poor degree of the achievable radius of the curvature in conventional steerable needles. Other ancillary limitations for some past steerable needle strategies include unwanted tissue damage and increased torsional friction that cause the rotation at the base to be out of sync with the tip's rotation angle. Developing new techniques that can compensate for some of the listed issues and move the steerable needles toward their clinical acceptance seems to be of utmost importance.

Declarations

References

1. Abayazid M, Roesthuis RJ, Reilink R, Misra S (2012) Integrating deflection models and image feedback for real-time flexible needle steering. IEEE Trans Rob 29(2):542–553
2. Abayazid M, Moreira P, Shahriari N, Patil S, Alterovitz R, Misra S (2015) Ultrasound-guided three-dimensional needle steering in biological tissue with curved surfaces. Med Eng Phys 37(1):145–150
3. Abayazid M, Kemp M, Misra S (2013) 3d flexible needle steering in soft-tissue phantoms using fiber Bragg grating sensors. In: 2013 IEEE international conference on robotics and automation. IEEE, pp 5843–5849
4. Abolhassani N, Patel R, Moallem M (2007) Needle insertion into soft tissue: a survey. Med Eng Phys 29(4):413–431
5. Adebar TK, Okamura AM (2014) Recursive estimation of needle pose for control of 3d-ultrasound-guided robotic needle steering. In: 2014 IEEE/RSJ international conference on intelligent robots and systems. IEEE, pp 4303–4308
6. Adebar TK, Fletcher AE, Okamura AM (2014) 3-d ultrasound-guided robotic needle steering in biological tissue. IEEE Trans Biomed Eng 61(12):2899–2910
7. Adebar TK, Greer JD, Laeseke PF, Hwang GL, Okamura AM (2015) Methods for improving the curvature of steerable needles in biological tissue. IEEE Trans Biomed Eng 63(6):1167–1177
8. Adebar TK, Greer JD, Laeseke PF, Hwang GL, Okamura AM (2016) Methods for improving the curvature of steerable needles in biological tissue. IEEE Trans Biomed Eng 63(6):1167–1177
9. Alterovitz R, Goldberg KY, Pouliot J, Hsu IC (2008) Sensorless motion planning for medical needle insertion in deformable tissues. IEEE Trans Inf Technol Biomed 13(2):217–225

10. Alterovitz R, Goldberg K, Okamura A (2005) Planning for steerable bevel-tip needle insertion through 2d soft tissue with obstacles. In: Proceedings of the 2005 IEEE international conference on robotics and automation. IEEE, pp 1640–1645

11. Alterovitz R, Lim A, Goldberg K, Chirikjian GS, Okamura AM (2005) Steering flexible needles under Markov motion uncertainty. In: 2005 IEEE/RSJ international conference on intelligent robots and systems. IEEE, pp 1570–1575

12. Alterovitz R, Siméon T, Goldberg K (2007) The stochastic motion roadmap: a sampling framework for planning with Markov motion uncertainty. Robotics: In Science and Systems, Atlanta, United States. ffhal-01987480f

13. Ayvali E, Liang CP, Ho M, Chen Y, Desai JP (2012) Towards a discretely actuated steerable cannula for diagnostic and therapeutic procedures. Int J Robot Res 31(5):588–603

14. Babaiasl M, Boccelli S, Chen Y, Yang, F, Ding JL, Swensen JP (2020) Predictive mechanics based model for depth of cut (DOC) of waterjet in soft tissue for waterjet-assisted medical applications. Medical & Biological Engineering & Computing 58(8): 1845–1872

15. Babaiasl M, Yang F, Boccelli S, Swensen JP (2020) Fracture-directed waterjet needle steering: design, modeling, and path planning. In: 2020 international conference on biomedical robotics and biomechatronics (BioRob). IEEE

16. Babaiasl M, Yang F, Chen Y, Ding JL, Swensen JP (2019) Predicting depth of cut of water-jet in soft tissue simulants based on finite element analysis with the application to fracture-directed water-jet steerable needles. In: 2019 international symposium on medical robotics (ISMR). IEEE, pp 1–7

17. Babaiasl M, Yang F, Swensen JP (2018) Towards water-jet steerable needles. In: 2018 7th IEEE international conference on biomedical robotics and biomechatronics (Biorob). IEEE, pp 601–608

18. Babaiasl M, Yang F, Swensen JP (2020) Duty cycling of waterjet can improve steerability and radius-of-curvature (roc) for waterjet steerable needles. In: 2020 international symposium on medical robotics (ISMR). IEEE

19. Bernardes MC, Adorno BV, Poignet P, Borges GA (2012) Semi-automatic needle steering system with robotic manipulator. In: 2012 IEEE international conference on robotics and automation. IEEE, pp 1595–1600

20. Bernardes MC, Adorno BV, Poignet P, Zemiti N, Borges GA (2011) Adaptive path planning for steerable needles using duty-cycling. In: 2011 IEEE/RSJ international conference on intelligent robots and systems. IEEE, pp 2545–2550

21. Bernardes M, Adorno BV, Poignet P, Borges G (2013) Robot-assisted automatic insertion of steerable needles with closed-loop imaging feedback and intraoperative trajectory replanning. Mechatronics 23(6):630–645

22. Bernardes MC, Adorno BV, Borges GA, Poignet P (2014) 3d robust online motion planning for steerable needles in dynamic workspaces using duty-cycled rotation. J Control Autom Electr Syst 25(2):216–227

23. Black RJ, Ryu S, Moslehi B, Costa JM (2014) Characterization of optically actuated MRI-compatible active needles for medical interventions. In: Behavior and mechanics of multifunctional materials and composites 2014, vol 9058. International Society for Optics and Photonics, p 90580J

24. Bui VK, Park S, Park JO, Ko SY (2016) A novel curvature-controllable steerable needle for percutaneous intervention. Proc Inst Mech Eng [H] 230(8):727–738

25. Burgner J, Swaney PJ, Lathrop RA, Weaver KD, Webster RJ (2013) Debulking from within: a robotic steerable cannula for intracerebral hemorrhage evacuation. IEEE Trans Biomed Eng 60(9):2567–2575

26. Burrows C, Secoli R, y Baena FR (2013) Experimental characterisation of a biologically inspired 3D steering needle. In: 2013 13th international conference on control, automation and systems (ICCAS 2013). IEEE, pp 1252–1257

27. Cannon LM, Fagan AJ, Browne JE (2011) Novel tissue mimicking materials for high frequency breast ultrasound phantoms. Ultrasound Med Biol 37(1):122–135

28. Ceh D, Peters TM, Chen EC (2015) Acoustic characterization of polyvinyl chloride and self-healing silicone as phantom materials. In: Medical imaging 2015: physics of medical imaging, vol 9412. International Society for Optics and Photonics, p 94123G

29. Chatelain P, Krupa A, Navab N (2015) 3d ultrasound-guided robotic steering of a flexible needle via visual servoing. In: 2015 IEEE international conference on robotics and automation (ICRA). IEEE, pp 2250–2255

30. Chen AI, Balter ML, Chen MI, Gross D, Alam SK, Maguire TJ, Yarmush ML (2016) Multilayered tissue mimicking skin and vessel phantoms with tunable mechanical, optical, and acoustic properties. Med Phys 43(6Part1):3117–3131

31. Chentanez N, Alterovitz R, Ritchie D, Cho L, Hauser KK, Goldberg K, Shewchuk JR, O'Brien JF (2009) Interactive simulation of surgical needle insertion and steering. In: ACM SIGGRAPH 2009 papers, pp 1–10

32. Datla NV, Hutapea P (2015) Flexure-Based Active Needle for Enhanced Steering Within Soft Tissue. ASME J Med Devices 9(4): 041005

33. de Carvalho IM, De Matheo LL, Júnior JFSC, de Melo Borba C, von Krüger MA, Infantosi AFC, de Albuquerque Pereira WC (2016) Polyvinyl chloride plastisol breast phantoms for ultrasound imaging. Ultrasonics 70:98–106

34. De Falco I, Culmone C, Menciassi A, Dankelman J, van den Dobbelsteen JJ (2018) A variable stiffness mechanism for steerable percutaneous instruments: integration in a needle. Med Biol Eng Comput 56(12):2185–2199

35. de Jong TL, Pluymen LH, van Gerwen DJ, Kleinrensink GJ, Dankelman J, van den Dobbelsteen JJ (2017) PVA matches human liver in needle-tissue interaction. J Mech Behav Biomed Mater 69:223–228

36. Dehghan E, Salcudean SE (2009) Needle insertion parameter optimization for brachytherapy. IEEE Trans Rob 25(2):303–315

37. DiMaio SP, Salcudean S (2003) Needle steering and model-based trajectory planning. In: International conference on medical image computing and computer-assisted intervention. Springer, pp 33–40

38. DiMaio SP, Salcudean SE (2005) Interactive simulation of needle insertion models. IEEE Trans Biomed Eng 52(7):1167–1179

39. DiMaio SP, Salcudean SE (2005) Needle steering and motion planning in soft tissues. IEEE Trans Biomed Eng 52(6):965–974

40. Donder A, Baena FRY (2021) Kalman-filter-based, dynamic 3-d shape reconstruction for steerable needles with fiber bragg gratings in multicore fibers. IEEE Transactions on Robotics 38(4):2262–2275

41. Duindam V, Alterovitz R, Sastry S, Goldberg K (2008) Screw-based motion planning for bevel-tip flexible needles in 3D environments with obstacles. In: 2008 IEEE international conference on robotics and automation. IEEE, pp 2483–2488

42. Dupont PE, Lock J, Itkowitz B, Butler E (2009) Design and control of concentric-tube robots. IEEE Trans Rob 26(2):209–225

43. Dupont P, Gosline A, Vasilyev N, Lock J, Butler E, Folk C, Cohen A, Chen R, Schmitz G, Ren H, et al (2012) Concentric tube robots for minimally invasive surgery. In: Hamlyn symposium on medical robotics, vol 7, p 8

44. Duriez C, Guébert C, Marchal M, Cotin S, Grisoni L (2009) Interactive simulation of flexible needle insertions based on constraint models. In: International conference on medical image computing and computer-assisted intervention. Springer, pp 291–299

45. Engh JA, Podnar G, Kondziolka D, Riviere CN (2006) Toward effective needle steering in brain tissue. In: 2006 international conference of the IEEE engineering in medicine and biology society. IEEE, pp 559–562

46. Engh JA, Minhas DS, Kondziolka D, Riviere CN (2010) Percutaneous intracerebral navigation by duty-cycled spinning of flexible bevel-tipped needles. Neurosurgery 67(4):1117–1123

47. Fallahi B, Rossa C, Sloboda RS, Usmani N, Tavakoli M (2016) Sliding-based switching control for image-guided needle steering in soft tissue. IEEE Robot Autom Lett 1(2):860–867

48. Farrer AI, Odéen H, de Bever J, Coats B, Parker DL, Payne A, Christensen DA (2015) Characterization and evaluation of tissue-mimicking gelatin phantoms for use with MRGFUS. J Ther Ultrasound 3(1):9

49. Fonseca M, Zeqiri B, Beard P, Cox B (2016) Characterisation of a phantom for multiwavelength quantitative photoacoustic imaging. Phys Med Biol 61(13):4950

50. Forte AE, Galvan S, Manieri F, y Baena FR, Dini D (2016) A composite hydrogel for brain tissue phantoms. Mater Des 112:227–238

51. Frasson L, Ko S, Turner A, Parittotokkaporn T, Vincent JF, Rodriguez y Baena F (2010) Sting: a soft-tissue intervention and neurosurgical guide to access deep brain lesions through curved trajectories. Proc Inst Mech Eng Part H J Eng Med 224(6):775–788

52. Gerboni G, Greer JD, Laeseke PF, Hwang GL, Okamura AM (2017) Highly articulated robotic needle achieves distributed ablation of liver tissue. IEEE robotics and automation letters 2(3):1367–1374

53. Gilbert HB, Neimat J, Webster RJ (2015) Concentric tube robots as steerable needles: achieving follow-the-leader deployment. IEEE Trans Rob 31(2):246–258

54. Glozman D, Shoham M (2007) Image-guided robotic flexible needle steering. IEEE Trans Robot 23(3):459–467

55. Glozman D, Shoham M (2007) Image-guided robotic flexible needle steering. IEEE Trans Rob 23(3):459–467

56. Glozman D, Shoham M (2004) Flexible needle steering and optimal trajectory planning for percutaneous therapies. In: International conference on medical image computing and computer-assisted intervention. Springer, pp 137–144

57. Goksel O, Dehghan E, Salcudean SE (2009) Modeling and simulation of flexible needles. Med Eng Phys 31(9):1069–1078

58. Grimm PD, Blasko JC, Sylvester JE, Meier RM, Cavanagh W (2001) 10-year biochemical (prostate-specific antigen) control of prostate cancer with 125i brachytherapy. Int J Radiat Oncol* Biol* Phys 51(1):31–40

59. Ha J, Fagogenis G, Dupont PE (2018) Modeling tube clearance and bounding the effect of friction in concentric tube robot kinematics. IEEE Trans Rob 35(2):353–370

60. Haddadi A, Hashtrudi-Zaad K (2011) Development of a dynamic model for bevel-tip flexible needle insertion into soft tissues. In: 2011 annual international conference of the IEEE engineering in medicine and biology society. IEEE, pp 7478–7482

61. Hamzé N, Peterlík I, Cotin S, Essert C (2016) Preoperative trajectory planning for percutaneous procedures in deformable environments. Comput Med Imaging Graph 47:16–28

62. Hauser K, Alterovitz R, Chentanez N, Okamura A, Goldberg K (2009) Feedback control for steering needles through 3d deformable tissue using helical paths. In: Robotics science and systems: online proceedings, vol 37

63. Hungr N, Long JA, Beix V, Troccaz J (2012) A realistic deformable prostate phantom for multimodal imaging and needle-insertion procedures. Med Phys 39(4):2031–2041

64. Ilami M, Ahmed RJ, Petras A, Beigzadeh B, Marvi H (2020) Magnetic needle steering in soft phantom tissue. Sci Rep 10(1):1–11

65. Jiang S, Liu S, Feng W (2011) PVA hydrogel properties for biomedical application. J Mech Behav Biomed Mater 4(7):1228–1233

66. Jiang S, Su Z, Wang X, Liu S, Yu Y (2013) Development of a new tissue-equivalent material applied to optimizing surgical accuracy. Mater Sci Eng C 33(7):3768–3774

67. Jiang S, Hata N, Kikinis R (2008) Needle insertion simulation for image-guided brachytherapy of prostate cancer. In: 2008 2nd international conference on bioinformatics and biomedical engineering. IEEE, pp 1682–1685

68. Joinié-Maurin M, Bayle B, Gangloff J (2011) Force feedback teleoperation with periodical disturbance compensation. In: 2011 IEEE international conference on robotics and automation. IEEE, pp 4828–4833

69. Kallem V, Cowan NJ (2007) Image-guided control of flexible bevel-tip needles. In: Proceedings 2007 IEEE International Conference on Robotics and Automation. IEEE, pp 3015–3020

70. Kato T, Okumura I, Song SE, Golby AJ, Hata N (2014) Tendon-driven continuum robot for endoscopic surgery: preclinical development and validation of a tension propagation model. IEEE/ASME Trans Mechatron 20(5):2252–2263

71. Kaye DR, Stoianovici D, Han M (2014) Robotic ultrasound and needle guidance for prostate cancer management: review of the contemporary literature. Curr Opin Urol 24(1):75

72. Khadem M, Rossa C, Usmani N, Sloboda RS, Tavakoli M (2016) A two-body rigid/flexible model of needle steering dynamics in soft tissue. IEEE/ASME Trans Mechatron 21(5):2352–2364

73. Khadem M, Rossa C, Usmani N, Sloboda RS, Tavakoli M (2017) Robotic-assisted needle steering around anatomical obstacles using notched steerable needles. IEEE J Biomed Health Inform 22(6):1917–1928

74. Khadem M, Fallahi B, Rossa C, Sloboda RS, Usmani N, Tavakoli M (2015) A mechanics-based model for simulation and control of flexible needle insertion in soft tissue. In: 2015 IEEE international conference on robotics and automation (ICRA. IEEE), pp 2264–2269

75. Khadem M, Rossa C, Usmani N, Sloboda RS, Tavakoli M (2016) Introducing notched flexible needles with increased deflection curvature in soft tissue. In: Advanced intelligent mechatronics (AIM), 2016 IEEE International Conference on. IEEE, pp 1186–1191

76. Kim Y, Parada GA, Liu S, Zhao X (2019) Ferromagnetic soft continuum robots. Science. Robotics 4(33):eaax7329

77. Ko SY, y Baena FR (2012) Toward a miniaturized needle steering system with path planning for obstacle avoidance. IEEE Trans Biomed Eng 60(4):910–917

78. Ko SY, y Baena FR (2012) Trajectory following for a flexible probe with state/input constraints: an approach based on model predictive control. Robot Auton Syst 60(4):509–521

79. Ko SY, Frasson L, y Baena FR (2011) Closed-loop planar motion control of a steerable probe with a "programmable bevel" inspired by nature. IEEE Trans Rob 27(5):970–983

80. Konh B, Honarvar M, Darvish K, Hutapea P (2017) Simulation and experimental studies in needle-tissue interactions. J Clin Monit Comput 31(4):861–872

81. Konh B, Sasaki D, Podder TK, Ashrafiuon H (2020) 3d manipulation of an active steerable needle via actuation of multiple SMA wires. Robotica 38(3):410–426

82. Konh B, Motalleb M (2017) Evaluating the performance of an advanced smart needle prototype inside tissue. In: Active and passive smart structures and integrated systems 2017, vol 10164. International Society for Optics and Photonics, p 101640G

83. Konh B, Podder TK (2017) Design and fabrication of a robust active needle using SMA wires. In: 2017 Design of medical devices conference. American Society of Mechanical Engineers Digital Collection

84. Krupa A (2014) A new duty-cycling approach for 3d needle steering allowing the use of the classical visual servoing framework for targeting tasks. In: 5th IEEE RAS/EMBS international conference on biomedical robotics and biomechatronics. IEEE, pp 301–307

85. Lee J, Park W (2014) A probability-based path planning method using fuzzy logic. In: 2014 IEEE/RSJ international conference on intelligent robots and systems. IEEE, pp 2978–2984

86. Lee J, Wang J, Park W (2018) Efficient Mechanism Design and Systematic Operation Planning for Tube-Wire Flexible Needles. ASME. J. Mechanisms Robotics 10(6): 065001

87. Lehmann T, Sloboda R, Usmani N, Tavakoli M (2018) Model-based needle steering in soft tissue via lateral needle actuation. IEEE Robot Autom Lett 3(4):3930–3936

88. Leibinger A, Forte AE, Tan Z, Oldfield MJ, Beyrau F, Dini D, y Baena FR (2016) Soft tissue phantoms for realistic needle insertion: a comparative study. Ann Biomed Eng 44(8):2442–2452

89. Lencioni R, Crocetti L, Della Pina MC, Cioni D (2009) Percutaneous image-guided radiofrequency ablation of liver tumors. Abdom Imaging 34(5):547–556

90. Lezcano DA, Iordachita II, Kim JS (2020) Trajectory generation of FBG-sensorized needles for insertions into multi-layer tissue. In: 2020 IEEE SENSORS. IEEE, pp 1–4

91. Li P, Jiang S, Yu Y, Yang J, Yang Z (2015) Biomaterial characteristics and application of silicone rubber and PVA hydrogels mimicked in organ groups for prostate brachytherapy. J Mech Behav Biomed Mater 49:220–234

92. Li W, Belmont B, Shih A (2015) Design and manufacture of polyvinyl chloride (PVC) tissue mimicking material for needle insertion. Procedia Manuf 1:866–878

93. Li W, Belmont B, Greve JM, Manders AB, Downey BC, Zhang X, Xu Z, Guo D, Shih A (2016) Polyvinyl chloride as a multimodal tissue-mimicking material with tuned mechanical and medical imaging properties. Med Phys 43(10):5577–5592

94. Li P, Yang Z, Jiang S (2018) Needle-tissue interactive mechanism and steering control in image-guided robot-assisted minimally invasive surgery: a review. Med Biol Eng Comput 56(6):931–949

95. Li P, Yang Z, Jiang S (2018) Tissue mimicking materials in image-guided needle-based interventions: a review. Mater Sci Eng C 93:1116–1131

96. Liu Y, Ge Z, Yang S, Walker ID, Ju Z (2019) Elephant's trunk robot: an extremely versatile under-actuated continuum robot driven by a single motor. J Mech Robot 11(5)

97. Lobo JR, Moradi M, Chng N, Dehghan E, Morris WJ, Fichtinger G, Salcudean SE (2011) Use of needle track detection to quantify the displacement of stranded seeds following prostate brachytherapy. IEEE Trans Med Imaging 31(3):738–748

98. Losey DP, York PA, Swaney PJ, Burgner J, Webster III R.J (2013) A flexure-based wrist for needle-sized surgical robots. In: Medical imaging 2013: image-guided procedures, robotic interventions, and modeling, vol 8671. International Society for Optics and Photonics, p 86711G

99. Lyons LA, Webster RJ, Alterovitz R (2010) Planning active cannula configurations through tubular anatomy. In: 2010 IEEE international conference on robotics and automation. IEEE, pp 2082–2087

100. Maghsoudi A, Jahed M (2012) Needle dynamics modelling and control in prostate brachytherapy. IET Control Theory Appl 6(11):1671–1681

101. Majewicz A, Marra SP, Van Vledder MG, Lin M, Choti MA, Song DY, Okamura AM (2012) Behavior of tip-steerable needles in ex vivo and in vivo tissue. IEEE Trans Biomed Eng 59(10):2705–2715

102. Majewicz A, Okamura AM (2013) Cartesian and joint space teleoperation for nonholonomic steerable needles. In: 2013 world haptics conference (WHC). IEEE, pp 395–400

103. Majewicz A, Siegel JJ, Stanley AA, Okamura AM (2014) Design and evaluation of duty-cycling steering algorithms for robotically-driven steerable needles. In: 2014 IEEE international conference on robotics and automation (ICRA). IEEE, pp 5883–5888

104. Majewicz A, Wedlick TR, Reed KB, Okamura AM (2010) Evaluation of robotic needle steering in ex vivo tissue. In: 2010 IEEE international conference on robotics and automation. IEEE, pp 2068–2073

105. Mallapragada VG, Sarkar N, Podder TK (2009) Robot-assisted real-time tumor manipulation for breast biopsy. IEEE Trans Rob 25(2):316–324

106. Matheson E, Secoli R, Burrows C, Leibinger A, Rodriguez y Baena F (2019) Cyclic motion control for programmable bevel-tip needles to reduce tissue deformation. J Med Robot Res 4(01):1842001

107. Meltsner M, Ferrier N, Thomadsen B (2007) Observations on rotating needle insertions using a brachytherapy robot. Phys Med Biol 52(19):6027

108. Mignon P, Poignet P, Troccaz J (2018) Automatic robotic steering of flexible needles from 3D ultrasound images in phantoms and ex vivo biological tissue. Ann Biomed Eng 46(9):1385–1396

109. Mignon P, Poignet P, Troccaz J (2016) Beveled-tip needle-steering using 3d ultrasound, mechanical-based Kalman filter and curvilinear ROI prediction. In: 2016 14th international conference on control, automation, robotics and vision (ICARCV). IEEE, pp 1–6

110. Minhas DS, Engh JA, Fenske MM, Riviere CN (2007) Modeling of needle steering via duty-cycled spinning. In: 2007 29th annual international conference of the IEEE engineering in medicine and biology society. IEEE, pp 2756–2759

111. Minton JA, Iravani A, Yousefi AM (2012) Improving the homogeneity of tissue-mimicking cryogel phantoms for medical imaging. Med Phys 39(11):6796–6807

112. Misra S, Reed KB, Schafer BW, Ramesh K, Okamura AM (2010) Mechanics of flexible needles robotically steered through soft tissue. Int J Robot Res 29(13):1640–1660

113. Misra S, Reed KB, Douglas AS, Ramesh K, Okamura AM (2008) Needle-tissue interaction forces for bevel-tip steerable needles. In: Biomedical robotics and biomechatronics, 2008. BioRob 2008. 2nd IEEE RAS & EMBS international conference on. IEEE, pp 224–231

114. Misra S, Reed KB, Schafer BW, Ramesh K, Okamura AM (2009) Observations and models for needle-tissue interactions. In: 2009 IEEE international conference on robotics and automation. IEEE, pp 2687–2692

115. Mora OC, Zanne P, Zorn L, Nageotte F, Zulina N, Gravelyn S, Montgomery P, de Mathelin M, Dallemagne B, Gora MJ (2020) Steerable oct catheter for real-time assistance during teleoperated endoscopic treatment of colorectal cancer. Biomed Opt Express 11(3):1231–1243

116. Moreira P, Misra S (2015) Biomechanics-based curvature estimation for ultrasound-guided flexible needle steering in biological tissues. Ann Biomed Eng 43(8):1716–1726

117. Moreira P, Patil S, Alterovitz R, Misra S (2014) Needle steering in biological tissue using ultrasound-based online curvature estimation. In: 2014 IEEE international conference on robotics and automation (ICRA). IEEE, pp 4368–4373

118. Narayan M, Choti MA, Fey AM (2019) Data-driven detection of needle buckling events in robotic needle steering. J Med Robot Res 4(02):1850005

119. Neubach Z, Shoham M (2009) Ultrasound-guided robot for flexible needle steering. IEEE Trans Biomed Eng 57(4):799–805

120. O'Brien K, Boyer ZR, Mart BG, Brolliar CT, Carroll TL, Fichera L (2019) Towards flexible steerable instruments for office-based laryngeal surgery. In: 2019 design of medical devices conference. American Society of Mechanical Engineers Digital Collection

121. Okamura AM, Simone C, O'leary MD (2004) Force modeling for needle insertion into soft tissue. IEEE Trans Biomed Eng 51(10):1707–1716

122. Okazawa S, Ebrahimi R, Chuang J, Salcudean SE, Rohling R (2005) Hand-held steerable needle device. IEEE/ASME Trans Mechatron 10(3):285–296

123. Park YL, Elayaperumal S, Daniel B, Ryu SC, Shin M, Savall J, Black RJ, Moslehi B, Cutkosky MR (2010) Real-time estimation of 3-d needle shape and deflection for MRI-guided interventions. IEEE/ASME Trans Mechatron 15(6):906–915

124. Park W, Kim JS, Zhou Y, Cowan NJ, Okamura AM, Chirikjian GS (2005) Diffusion-based motion planning for a nonholonomic flexible needle model. In: Proceedings of the 2005 ieee international conference on robotics and automation. IEEE, pp 4600–4605

125. Park W, Reed KB, Okamura AM, Chirikjian GS (2010) Estimation of model parameters for steerable needles. In: 2010 IEEE international conference on robotics and automation. IEEE, pp 3703–3708

126. Patel NA, van Katwijk T, Li G, Moreira P, Shang W, Misra S, Fischer GS (2015) Closed-loop asymmetric-tip needle steering under continuous intraoperative MRI guidance. In: 2015 37th annual international conference of the IEEE engineering in medicine and biology society (EMBC). IEEE, pp 4869–4874

127. Patil S et al (2011) Motion planning under uncertainty in highly deformable environments. In: Robotics science and systems: online proceedings

128. Patil S, Burgner J, Webster RJ, Alterovitz R (2014) Needle steering in 3-d via rapid replanning. IEEE Trans Rob 30(4):853–864

129. Patil S, Alterovitz R (2010) Interactive motion planning for steerable needles in 3d environments with obstacles. In: 2010 3rd IEEE RAS & embs international conference on biomedical robotics and biomechatronics. IEEE, pp 893–899

130. Piccin O, Barbe L, Bayle B, De Mathelin M, Gangi A (2009) A force feedback teleoperated needle insertion device for percutaneous procedures. Int J Robot Res 28(9):1154–1168

131. Pratt RL, Petruska AJ (2022) Empirically comparing magnetic needle steering models using expectation-maximization. Robotics 11(2):49

132. Reed KB, Kallem V, Alterovitz R, Goldbergxz K, Okamura AM, Cowan NJ (2008) Integrated planning and image-guided control for planar needle steering. In: 2008 2nd IEEE RAS & EMBS international conference on biomedical robotics and biomechatronics. IEEE, pp 819–824

133. Reed KB, Okamura AM, Cowan NJ (2009) Controlling a robotically steered needle in the presence of torsional friction. In: 2009 IEEE international conference on robotics and automation. IEEE, pp 3476–3481

134. Reed KB, Okamura AM, Cowan NJ (2009) Modeling and control of needles with torsional friction. IEEE Trans Biomed Eng 56(12):2905–2916

135. Reed KB, Okamura AM, Cowan NJ (2009) Modeling and control of needles with torsional friction. IEEE Trans Biomed Eng 56(12):2905–2916. https://doi.org/10.1109/TBME.2009.2029240

136. Reed KB, Majewicz A, Kallem V, Alterovitz R, Goldberg K, Cowan NJ, Okamura AM (2011) Robot-assisted needle steering. IEEE Robot Autom Mag 18(4):35–46

137. Ritter RC, Quate EG, Gillies GT, Grady MS, Howard M, Broaddus WC (1998) Measurement of friction on straight catheters in in vitro brain and phantom material. IEEE Trans Biomed Eng 45(4):476–485

138. Roesthuis RJ, Abayazid M, Misra S (2012) Mechanics-based model for predicting in-plane needle deflection with multiple bends. In: 2012 4th IEEE RAS & EMBS international conference on biomedical robotics and biomechatronics (BioRob). IEEE, pp 69–74

139. Roesthuis RJ, van de Berg NJ, van den Dobbelsteen JJ, Misra S (2015) Modeling and steering of a novel actuated-tip needle through a soft-tissue simulant using fiber Bragg grating sensors. In: Robotics and automation (ICRA), 2015 IEEE international conference on. IEEE, pp 2283–2289

140. Romano JM, Webster RJ, Okamura AM (2007) Teleoperation of steerable needles. In: Proceedings 2007 IEEE international conference on robotics and automation. IEEE, pp 934–939

141. Ros-Freixedes L, Gao A, Liu N, Shen M, Yang GZ (2019) Design optimization of a contact-aided continuum robot for endobronchial interventions based on anatomical constraints. Int J Comput Assist Radiol Surg 14(7):1137–1146

142. Rucker DC, Webster RJ (2008) Mechanics-based modeling of bending and torsion in active cannulas. In: 2008 2nd IEEE RAS & EMBS international conference on biomedical robotics and biomechatronics. IEEE, pp 704–709

143. Rucker DC, Das J, Gilbert HB, Swaney PJ, Miga MI, Sarkar N, Webster RJ (2013) Sliding mode control of steerable needles. IEEE Trans Rob 29(5):1289–1299

144. Ryou M, Benias PC, Kumbhari V (2020) Initial clinical experience of a steerable access device for EUS-guided biliary drainage. Gastrointest Endosc 91(1):178–184

145. Ryu SC, Quek ZF, Koh JS, Renaud P, Black RJ, Moslehi B, Daniel BL, Cho KJ, Cutkosky MR (2014) Design of an optically controlled MR-compatible active needle. IEEE Trans Rob 31(1):1–11

146. Scali M, Kreeft D, Breedveld P, Dodou D (2017) Design and evaluation of a wasp-inspired steerable needle. In: Bioinspiration, Biomimetics, and Bioreplication 2017, vol 10162. International Society for Optics and Photonics, p 1016207

147. Scali M, Veldhoven PA, Henselmans PW, Dodou D, Breedveld P (2019) Design of an ultra-thin steerable probe for percutaneous interventions and preliminary evaluation in a gelatine phantom. PloS one 14(9): p.e0221165

148. Sears P, Dupont P (2006) A steerable needle technology using curved concentric tubes. In: 2006 IEEE/RSJ international conference on intelligent robots and systems. IEEE, pp 2850–2856

149. Secoli R, y Baena FR (2013) Closed-loop 3d motion modeling and control of a steerable needle for soft tissue surgery. In: 2013 IEEE international conference on robotics and automation. IEEE, pp 5831–5836

150. Seifabadi R, Song SE, Krieger A, Cho NB, Tokuda J, Fichtinger G, Iordachita I (2012) Robotic system for MRI-guided prostate biopsy: feasibility of teleoperated needle insertion and ex vivo phantom study. Int J Comput Assist Radiol Surg 7(2):181–190

151. Seifabadi R, Aalamifar F, Iordachita I, Fichtinger G (2016) Toward teleoperated needle steering under continuous MRI guidance for prostate percutaneous interventions. Int J Med Robot Comput Assist Surg 12(3):355–369

152. Shahriari N, Heerink W, Van Katwijk T, Hekman E, Oudkerk M, Misra S (2017) Computed tomography (CT)-compatible remote center of motion needle steering robot: fusing CT images and electromagnetic sensor data. Med Eng Phys 45:71–77

153. Sheng J, Deaton NJ, Desai JP (2019) A large-deflection FBG bending sensor for SMA bending modules for steerable surgical robots. In: 2019 international conference on robotics and automation (ICRA). IEEE, pp 900–906

154. Sitzman BT, Uncles DR (1996) The effects of needle type, gauge, and tip bend on spinal needle deflection. Anesth Analg 82(2):297–301

155. Sun W, Alterovitz R (2014) Motion planning under uncertainty for medical needle steering using optimization in belief space. In: 2014 IEEE/RSJ international conference on intelligent robots and systems. IEEE, pp 1775–1781

156. Sung H, Ferlay J, Siegel RL, Laversanne M, Soerjomataram I, Jemal A, Bray F (2021) Global cancer statistics 2020: GLOBO-

CAN estimates of incidence and mortality worldwide for 36 cancers in 185 countries. CA Cancer J Clin 71(3): 209–249

157. Swaney PJ, Burgner J, Pheiffer TS, Rucker DC, Gilbert HB, Ondrake JE, Simpson AL, Burdette EC, Miga MI, Webster III RJ (2012) Tracked 3D ultrasound targeting with an active cannula. In: Medical imaging 2012: image-guided procedures, robotic interventions, and modeling, vol 8316. International Society for Optics and Photonics, p 83160R

158. Swaney PJ, Gilbert HB, Hendrick RJ, Commichau O, Alterovitz R, Webster III RJ (2015) Transoral steerable needles in the lung: How non-annular concentric tube robots can improve targeting. In: Hamlyn symposium. Medical robotics

159. Swaney PJ, Burgner J, Gilbert HB, Webster RJ (2012) A flexure-based steerable needle: high curvature with reduced tissue damage. IEEE Trans Biomed Eng 60(4):906–909

160. Swaney PJ, Mahoney AW, Hartley BI, Remirez AA, Lamers E, Feins RH, Alterovitz R, Webster RJ III (2017) Toward transoral peripheral lung access: combining continuum robots and steerable needles. J Med Robot Res 2(01):1750001

161. Swensen JP, Cowan NJ (2012) Torsional dynamics compensation enhances robotic control of tip-steerable needles. In: Robotics and automation (ICRA), 2012 IEEE international conference on. IEEE, 1601–1606

162. Swensen JP, Lin M, Okamura AM, Cowan NJ (2014) Torsional dynamics of steerable needles: modeling and fluoroscopic guidance. IEEE Trans Biomed Eng 61(11):2707–2717

163. Tang W, Wan TR (2014) Constraint-based soft tissue simulation for virtual surgical training. IEEE Trans Biomed Eng 61(11):2698–2706

164. Torabi M, Hauser K, Alterovitz R, Duindam V, Goldberg K (2009) Guiding medical needles using single-point tissue manipulation. In: 2009 IEEE international conference on robotics and automation. IEEE, pp 2705–2710

165. van de Berg NJ, van Gerwen DJ, Dankelman J, van den Dobbelsteen JJ (2014) Design choices in needle steering—a review. IEEE/ASME Trans Mechatron 20(5):2172–2183

166. van de Berg NJ, Dankelman J, van den Dobbelsteen JJ (2015) Design of an actively controlled steerable needle with tendon actuation and FBG-based shape sensing. Med Eng Phys 37(6):617–622

167. van de Berg NJ, Dankelman J, van den Dobbelsteen JJ (2017) Endpoint accuracy in manual control of a steerable needle. J Vasc Interv Radiol 28(2):276–283

168. van de Berg NJ, de Jong TL, van Gerwen DJ, Dankelman J, van den Dobbelsteen JJ (2017) The influence of tip shape on bending force during needle insertion. Sci Rep 7:40477

169. Van Den Berg J, Patil S, Alterovitz R, Abbeel P, Goldberg K (2010) LQG-based planning, sensing, and control of steerable needles. In: Algorithmic foundations of robotics IX. Springer, pp 373–389

170. Vandini A, Bergeles C, Lin FY, Yang GZ (2015) Vision-based intraoperative shape sensing of concentric tube robots. In: 2015 IEEE/RSJ international conference on intelligent robots and systems (IROS). IEEE, 2603–2610

171. Vogt WC, Jia C, Wear KA, Garra BS, Pfefer TJ (2016) Biologically relevant photoacoustic imaging phantoms with tunable optical and acoustic properties. J Biomed Opt 21(10):101405

172. Wan G, Wei Z, Gardi L, Downey DB, Fenster A (2005) Brachytherapy needle deflection evaluation and correction. Med Phys 32(4):902–909

173. Wang TW, Spector M (2009) Development of hyaluronic acid-based scaffolds for brain tissue engineering. Acta Biomater 5(7):2371–2384

174. Wang J, Ha J, Dupont PE (2019) Steering a multi-armed robotic sheath using eccentric precurved tubes. In: 2019 international conference on robotics and automation (ICRA). IEEE, pp 9834–9840

175. Wang J, Li X, Zheng J, Sun D (2013) Mechanics-based modeling of needle insertion into soft tissue. In: 2013 IEEE/ASME international conference on advanced intelligent mechatronics. IEEE, pp 38–43

176. Wang Y, Tai BL, Yu H, Shih AJ (2014) Silicone-Based Tissue-Mimicking Phantom for Needle Insertion Simulation. ASME. J. Med. Devices 8(2): 021001

177. Watts T, Secoli R, y Baena FR (2018) A mechanics-based model for 3-d steering of programmable bevel-tip needles. IEEE Trans Rob 35(2):371–386

178. Webster RJ, Memisevic J, Okamura AM (2005) Design considerations for robotic needle steering. In: Proceedings of the 2005 IEEE international conference on robotics and automation. IEEE, pp 3588–3594

179. Webster RJ, Okamura AM, Cowan NJ (2006) Toward active cannulas: miniature snake-like surgical robots. In: 2006 IEEE/RSJ international conference on intelligent robots and systems. IEEE, pp 2857–2863

180. Webster RJ, Romano JM, Cowan NJ (2008) Kinematics and calibration of active cannulas. In: 2008 IEEE international conference on robotics and automation. IEEE, pp 3888–3895

181. Webster RJ III, Kim JS, Cowan NJ, Chirikjian GS, Okamura AM (2006) Nonholonomic modeling of needle steering. Int J Robot Res 25(5–6):509–525

182. Webster RJ III, Romano JM, Cowan NJ (2008) Mechanics of precurved-tube continuum robots. IEEE Trans Rob 25(1):67–78

183. Wedlick TR, Okamura AM (2009) Characterization of pre-curved needles for steering in tissue. In: Engineering in medicine and biology society, 2009. EMBC 2009. Annual International Conference of the IEEE. IEEE, pp 1200–1203

184. Wellborn PS, Swaney PJ, Webster RJ (2016) Curving clinical biopsy needles: can we steer needles and still obtain core biopsy samples? J Med Devices 10(3): 030904

185. Wood NA, Lehocky CA, Riviere CN (2013) Algorithm for three-dimensional control of needle steering via duty-cycled rotation. In: 2013 IEEE international conference on mechatronics (ICM). IEEE, pp 237–241

186. Wood NA, Shahrour K, Ost MC, Riviere CN (2010) Needle steering system using duty-cycled rotation for percutaneous kidney access. In: 2010 annual international conference of the IEEE engineering in medicine and biology. IEEE, pp 5432–5435

187. Xu J, Duindam V, Alterovitz R, Goldberg K (2008) Motion planning for steerable needles in 3d environments with obstacles using rapidly-exploring random trees and backchaining. In: 2008 IEEE international conference on automation science and engineering. IEEE, pp 41–46

188. Yamaguchi S, Tsutsui K, Satake K, Morikawa S, Shirai Y, Tanaka HT (2014) Dynamic analysis of a needle insertion for soft materials: arbitrary Lagrangian–Eulerian-based three-dimensional finite element analysis. Comput Biol Med 53:42–47

189. Yan KG, Podder T, Yu Y, Liu TI, Cheng CW, Ng WS (2008) Flexible needle-tissue interaction modeling with depth-varying mean parameter: preliminary study. IEEE Trans Biomed Eng 56(2):255–262

190. Yang F, Babaiasl M, Swensen JP (2019) Fracture-directed steerable needles. J Med Robot Res 4(01):1842002

191. Zell K, Sperl JI, Vogel MW, Niessner R, Haisch C (2007) Acoustical properties of selected tissue phantom materials for ultrasound imaging. Phys Med Biol 52(20):N475

192. Zhou Y, Thiruvalluvan K, Krzeminski L, Moore WH, Xu Z, Liang Z (2013) Ct-guided robotic needle biopsy of lung nodules with respiratory motion-experimental system and preliminary test. Int J Med Robot Comput Assist Surg 9(3):317–330

Mahdieh Babaiasl received her Ph.D. in Mechanical Engineering from Washington State University, USA, under the supervision of Dr. John Swensen. As her Ph.D. research, she has developed a mechanics-based model for cut-depth of waterjet in soft tissue as well as a waterjet steerable needle system to be used for robotics-assisted surgery. Her past research included designing and controlling an exoskeleton robot for upper-limb rehabilitation and a surgical robot. She serves as a reviewer for several prestigious journals and conferences, including IEEE RA-L, MBEC, IEEE access, TIMC, and COMPELECENG, among others. Her research interests are steerable needles, water-jet-assisted medical applications, and medical devices.

Fan Yang received his Ph.D. degree in Mechanical Engineering from Washington State University. He was a graduate research assistant in the Modeling, Motion, and Medical (M3) Robotics Laboratory under Dr. John P. Swensen's supervision. His research interests include steerable needles, continuum robotics, and medical devices.

John P. Swensen received his M.S. and Ph.D. degrees in Mechanical Engineering from the Johns Hopkins University, U.S.A, in 2009 and 2012, respectively. He is currently an Associate Professor in the School of Mechanical and Materials Engineering at Washington State University and the Director of the Modeling, Motion, and Medical (M3) Robotics Laboratory. The M3 Robotics Laboratory research focuses on research into compliant medical devices, including steerable needles and other tunably-compliant mechanisms.